Stellar Occultation Observations of Saturn's Upper Atmosphere

by

Asantha Roshan Cooray

Submitted in Partial Fulfillment of the Requirements for the Degree
of
Master of Science
in
Earth, Atmospheric, and Planetary Sciences
at the

Massachusetts Institute of Technology

June 1997

Signature of Author_____
Department of Earth, Atmospheric, and Planetary Sciences
May 8, 1997

Certified by_____
Professor James L. Elliot
Professor of Physics and Astronomy
Thesis Supervisor

Accepted by_____
Professor Thomas Jordan
Chairman
Department of Earth, Atmospheric, and Planetary Sciences

Stellar Occultation Observations of Saturn's Upper Atmosphere

by

Asantha Roshan Cooray

Submitted to the Department of Earth, Atmospheric, and Planetary
Sciences on May 8, 1997 in Partial Fulfillment of the
Requirements for the Degree of
Master of Science in Earth, Atmospheric, and Planetary Sciences.

ABSTRACT

We have analyzed three stellar occultation observations of Saturn's upper atmosphere during the years 1989 to 1995. These occultations probed the stratosphere at pressure levels about 0.5 to 20 μbars, intermediate to those probed by the Pioneer 11, Voyager I and II radio and ultraviolet occultations. The time span of the earlier occultations and the observation of a higher latitude occultation in 1995 can be used to detect any seasonal changes in the atmosphere, and temperature gradients between equator and higher latitudes.

Based on isothermal fits, we find a temperature of 137±10 K at the latitude of 84.4 degrees on Saturn at a pressure level of 1.54±0.09 μbar. In comparison to 28 Sgr temperature, we have not detected a major seasonal change between years 1989 and 1995 at the equator of Saturn. There is also no clear indication of a dependence of the stratospheric temperature on latitude. On the other hand, our temperature results confirm the general increase of temperature from tropopause to the lower thermosphere of Saturn. The 1994 light curve exhibits a strong absorption like feature over the whole altitude range probed. Using temperature gradient models we find a lapse rate of 0.38±0.07 K km^{-1}. However the light curve could have been affected by a thin cloud layer in our atmosphere, as observations were made under minimal weather conditions. The loss of signal during this event is also attributed to the movement of the occulted star out of data frames during the event.

The 1995 temperature profile covers both horizontal and vertical structure at a ratio of 8.25 to 1. This is the first temperature profile with a rather long horizontal structure of a polar region probed with a stellar occultation. The observed high-amplitude spikes in the light curve produce sudden temperature variations with amplitudes in the range 1 to 5 K. The temperature profile also exhibits a strong, local, variation of temperature of 14.5 K, over a small vertical distance of 18 km and a horizontal distance of 160 km. If the observed lapse rates in the temperature profile apply to the vertical direction only, then this region is super-adiabatic on scales of 3 to 4 km. More likely these thermal gradients are due to horizontal temperature variations.

Assuming that these non-isothermal features were caused by inertia-gravity waves propagating upward in the stratosphere and breaking up in the turbulent regions, we have estimated the heating caused by viscous dissipation. Order of magnitude calculations show that this heating rate is dominant, compared to UV and IR absorptions. The same waves are also considered to be the means of transporting aerosols that were observed with HST. We also examined a propagating wave interpretation for the temperature profiles near equator, where lapse rates never reach the adiabatic value. Inertia-gravity waves with wavelengths in the order of 140 km are consistent with the equatorial data, where as north polar data suggest wavelengths less than the scale height of 44.3 ± 4.2 Km.

A paper primarily based on the 1995 data is planned for publication. Most of the data presented on this thesis will be available on the AAS CD ROM.

Thesis Supervisor: James Elliot
Title: Professor of Physics and Earth, Atmospheric, and Planetary Sciences

Table of Contents

Chapter 1
Saturn Occultation Data

1.1 Introduction and Observations

Even though comprehensive occultation probing of the atmospheres of Jupiter (Hubbard *et al.* 1995), Neptune (Roques *et al.* 1994) and Uranus (Baron *et al.* 1989) have been made, the only successful Earth-based observation of Saturn's upper atmosphere prior to 1994 was the 3 July 1989 occultation of the bright star 28 Sgr (V=5.37, B–V=1.64, K=1.5, spectral class K4III). This occultation by Saturn, its rings, and Titan was observed by many professional and amateur astronomers both in the northern and southern hemispheres. The combined 28 Sgr data set has yielded very high-precision information on the structure of Saturn's rings (French *et al.* 1993; Hubbard *et al.* 1993; Harrington *et al.* 1993), Titan (Hubbard *et al.* 1990; Sicardy *et al.* 1990), and Saturn's atmosphere (Hubbard *et al.* 1997, hereafter referred to as H97).

Prior to the 28 Sgr observations, data on Saturn's atmosphere came from a series of radio (RSS) occultations below a radius of 60600 km (Lindal 1985) and ultraviolet (UVS) occultations above a radius of 61200 km (Smith *et al.* 1983) observed with the Pioneer 11, Voyager I and Voyager II spacecraft near Saturn. Results from the RSS occultations include a temperature of 145±4 K and a lapse rate of 0.8 K km^{-1} at the 1.3 bar level. The infrared imaging observations suggested that the atmosphere in the pressure range from 0.2 mbar to 1.3 bar is saturated with ammonia. At the tropopause, at a pressure level of 90 mbar, a temperature of 80 K at the equator and a temperature of 87 K at a latitude of –6 0° were found (Lindal *et al.* 1985). The UVS occultations (solar and δ Scorpii) suggested an upper atmospheric temperature of 420±30 K (Smith *et al.* 1983).

The recent analysis of the extensive atmospheric data set of 5 immersion and 9 emersion observations of the 28 Sgr event by H97 has allowed the authors to make profiles of number density, pressure and temperature as a function of altitude at latitudes

between $-15°$ and $+7°$. These visible and infrared occultation observations occur on Saturn at pressure levels between 1 to 100 μbar, about 400 km above the RSS occultations and 300 km below the UVS occultations.
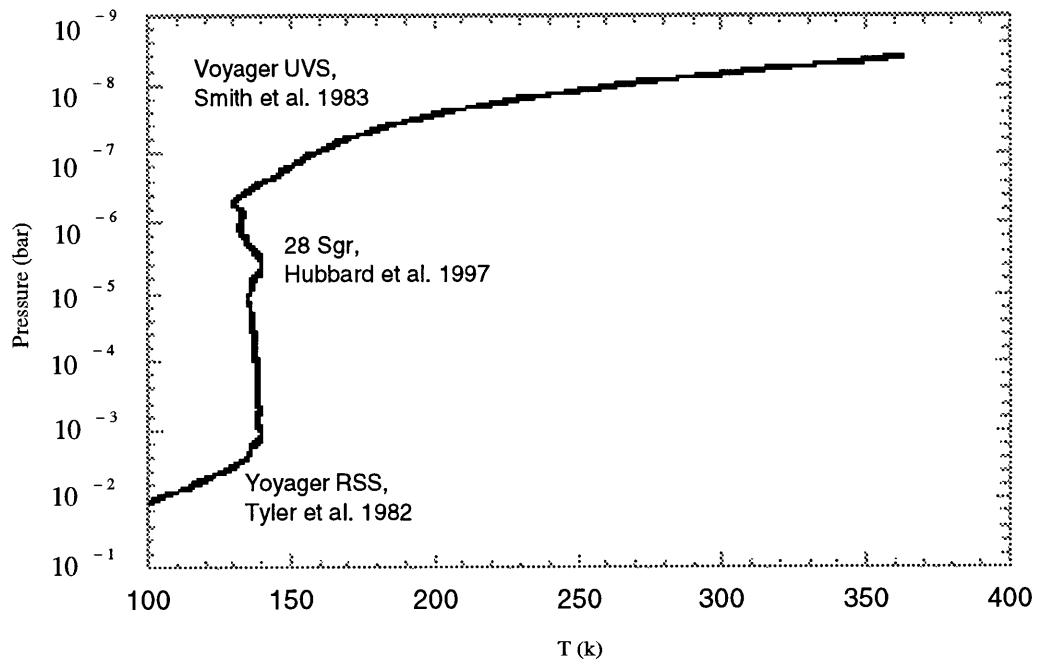

Figure 1.1 Summary of temperature measurements in Saturn's atmosphere. Here we have plotted the measured temperature vs. pressure based on different occultations: Voyager UVS, Voyager and Pioneer RSS and 28 Sgr. The pressure region of 10^{-6} to 10^{-4} bar is where infrared and visible occultations occur.

H97 used the 28 Sgr data to confirm the substantial equatorial bulge produced by high equatorial zonal winds, with velocities of 450 to 500 ms^{-1} near equator. These zonal winds were first observed with Voyager I, and were reconfirmed with Voyager II (Ingersoll and Pollard, 1982). The general result from the analysis of 28 Sgr data is that the atmospheric temperature is 141±10 K at the 1 μbar level, near equator. H97 combined the results from spacecraft observations and 28 Sgr analysis to create a model of Saturn's atmosphere. Figure 1.1 plots the temperature vs. pressure of this combined model.

Occultations of stars as bright as 28 Sgr by Saturn are rare. However, the availability of high-speed infrared detectors can be used to observe occultations by Saturn on a routine basis. An array can be used at absorption bands of molecular species in Saturn's atmosphere, such as wavelengths near K band (2.2μm) where CH_4 absorption is at its highest, or at 3.2μm, where there is a water-ice absorption band (making Saturn's rings appear dark) and a CH_4 absorption band (making Saturn appear dark).

With the hope of building an increasingly accurate orbital model for Saturn's rings, Bosh and McDonald (1992) predicted 203 potential stellar occultations by Saturn from the Hubble Space Telescope Guide Star Catalog (GSC). We picked several events in the years between 1994 and 1996 based on the location where event is visible and the predicted signal-to-noise ratio of the data. This thesis presents data and results from two such occultation observations. The first event, GSC5815-01190, occurred on September 18, 1994, and the second, GSC5249-01240, was observed during Saturn's solar ring plane crossing on November 20-21, 1995. In order to combine our results with those of H97, we have also analyzed the 28 Sgr atmospheric occultation observations at IRTF.

Infrared observations of the GSC5815-01190 occultation were made at IRTF using the NSFCAM by A. Bosh and J. Elliot, and visible observations were made at the U. of Hawaii 88 inch telescope using the MIT Portable CCD (PCCD) system by H. Hammel and J. Foust. Though a primary goal of this 1994 occultation observation was to obtain the hydrogen-to-helium ratio of Saturn's atmosphere through time delay of spikes as observed in light curves of two different wavelengths, clouds and high humidity permitted only emersion observations at IRTF.

7

The 1995 event, as described in section 1.3.3, was important because it occurred at the time of Saturn's ring-plane crossing and it had the slowest velocity of all the GSC occultation events predicted by Bosh and McDonald (1992). Though similar plans were made to observe this event in two wavelengths using the NSFCAM and the MIT PCCD (which was to be located on the optical port of the NSFCAM), only infrared observations were successful due to mechanical and focusing problems with the PCCD. As the emersion occurred during the day time, only immersion observations were recorded. This 1995 event was also observed with the Hubble Space Telescope Faint Object Spectrograph, and the data are being analyzed by J. Foust.

Other than the derivation of atmospheric structure parameters, stellar occultation observations can also be used to determine the shape of a planetary atmosphere. For example, a series of occultation observations was used by Baron *et al.* (1989) to predict the shape of Uranus' atmosphere even before the Voyager observations of Uranus. In this study we are concerned with the shape of Saturn's atmosphere for two reasons: (1) the November 20, 1995 GSC5249-01240 event occurred at latitudes ranging from $82.5°$ to $85.5°$ and east longitudes, based on prime meridian as defined by Desch and Kaiser (1981), from $21°$ to $32°$ on Saturn; Previously no occultation had been observed at a latitude higher than $25°$ or lower than $-66°$, and (2) for comparative purposes with the results of H97 and other studies on Saturn's atmosphere. In order to compare the 14 light curves, H97 defined an equivalent equatorial half-light level for all the 28 Sgr events, which was defined as the half-light radius of the event if it had occurred at the equator instead of at the observed latitude. To establish the equivalent equatorial half-light level one requires knowledge on Saturn's atmospheric shape at all latitudes based on the present data on zonal winds.

The aim of this thesis is to homogeneously analyze all occultation curves the MIT group have obtained, and to derive from each of them stratospheric temperature, pressure, number density and scale height profiles. Since different events were observed at different latitudes on Saturn, the variations in thermal structure of Saturn based on location (near-equator or high latitudes) are described, and possible implications for heating mechanisms in Saturn's stratosphere are discussed. Though two other publications exist on Saturn's atmosphere based on occultations (H97 and central flash analysis by Nicholson *et al.* 1995), there is no study done on Saturn's

atmosphere that directly suggests the existence of waves, either gravity or acoustic. We will reuse some of these published data together with new observations to investigate the different mechanisms of aerosol transfer between Saturn's stratosphere and troposphere. The μbar region, where stellar and infrared occultations are sensitive, is particularly interesting since radiative processes, like UV and IR absorptions by methane, acetylene and ethane, compete with other physical processes in the thermal balance of the upper atmosphere. Among others are the conductive heating from the thermosphere, wave diffusion processes, and heating from aerosols and from ionosphere through possible auroral activity at high latitudes. Understanding the contributions from each of these different effects to Saturn's overall heat budget is important.

1.2 Saturn's Shape

The shape of Saturn's atmosphere can be determined from its outer gravitational field due to the mass distribution and from the centrifugal forces due to the rotation. Past observations using Pioneer 11, Voyager 1 and Voyager 2 spacecraft have shown that the atmosphere is pronouncedly nonspherical due to rapid rotation and zonal winds. The zonal winds were found to distort the planet due to the underlying uniform rotation, which corresponds to the magnetic-field rotation period (Lindal et al 1985). The departures from the uniform behavior at different pressure levels of the atmosphere can predict the existence of zonal winds at that level. For Saturn, spacecraft occultation data were used by Lindal *et al.* (1985) to identify and model the deviations from a calculated reference geoid defined by the planet's external gravity field due to the magnetic field rotation. A term was introduced to represent the eastward zonal-wind velocities as determined through Voyager I and II images at a pressure level of 1 bar. The resulting shape due to zonal winds plus uniform rotation deviated approximately 2% from the shape due to only uniform rotation.

An accurate determination of the differential rotation and the shape can easily be used to constrain planetary interior models. Hubbard and Stevenson (1984) have shown that Saturn's differential rotation due to zonal winds implies that the planet is rotating as individual cylinders and that these rotations change the values of gravitational moments by increasing the gravitational harmonics J2 and J4 by 0.5%

9

and 2.2% respectively of values with no contribution due to zonal winds.

Though Saturn's shape at the 1 bar level is constrained through the spacecraft data at few points, it is not exactly clear how the wind velocities at the 1 bar level affect the figure at higher altitudes. For example, at the μbar region where stellar occultations occur, there is still a slight difference as to Saturn's shape based on 28 Sgr occultation data by H97 and the central flash data of the same event as analyzed by Nicholson *et al.* (1995).

The analysis of the total 28 Sgr data set of 5 immersion and 9 emersion observations by H97 included the effect of wind velocities at 1 bar level by an extrapolation to the μbar level through the assumption of cylindrical rotation. The investigators found that the nonsphericity of Saturn's atmosphere due to zonal winds has a considerable effect in their data, whereas the central flash data indicated some decay of zonal winds with height above the 1.5 mbar level. The difference in wind velocities as required by different data sets can be due to the different location of the events. The 14 events observed during the 1989 July 3 occultation occurred in between –15 to +7 degrees from Saturn's planetocentric latitudes and the central flash probed higher latitudes in the range +25 to +70 degrees. The zonal wind velocities at latitudes between –70 and +70 degrees at the 1 bar level have been well determined. Though the shape of Saturn at this level has been well constrained through several spacecraft radio occultations, the only high latitude occultation observed so far was by Voyager I at a latitude of 74.5 S.

Nicholson *et al.* (1995) found that their central flash data imply a uniform wind speed of 40 ms^{-1} at the 1 mbar level between +25 and +70 degrees latitude. In contrast to the zonal wind profiles at the cloud levels a few hundred kilometers below this level, the authors suggested that at mid-latitudes winds decay with height above the troposphere to a non zero constant value at the region probed by central flashes.
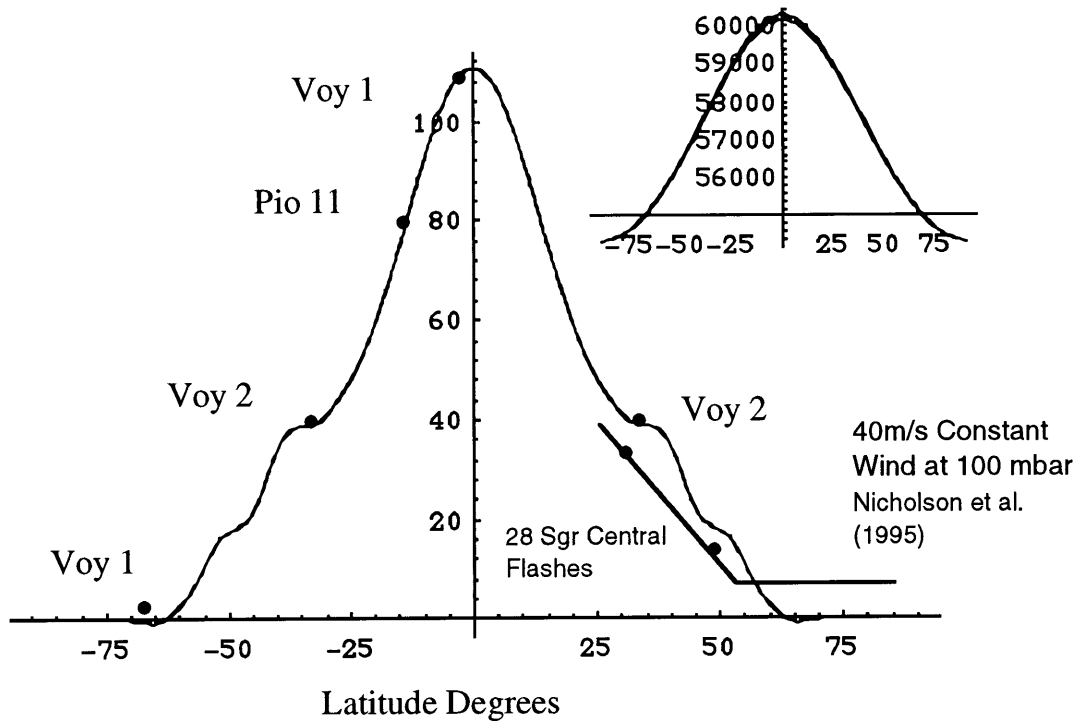
Figure 1.2 The shape of Saturn's atmosphere at the 1 bar level. Shown here is the altitude above the reference geoid. The reference geoid is defined as the shape due to the uniform rotation (wind-free). The inset plots the geoid and the shape due to zonal winds. The centripetal accelerations involved with zonal winds change the effective potential field of Saturn, and when the winds are taken into account, a constant pressure surface is displaced from the uniform rotation geoid by about 110 km at the 1 bar level, and by about 122 km at 2 μbar level. Also shown are the locations of the observed occultations from spacecraft data and the two locations of the four central flashes observed during the 28 Sgr occultation (Nicholson *et al.* 1995). The straight line joining these two locations has been suggested by the above authors as an alternate shape at the 100 mbar level. The difference between the predicted shape based on spacecraft occultations and the central flash data suggests the decay of winds between the two levels probed by different data sets.

In Figure 1.2 we have summarized the present knowledge of Saturn's shape based on Pioneer 11, Voyager I and Voyager II occultations. All of the events observed by spacecrafts occurred at a pressure level of 1 bar. Also plotted on Figure 1.2 are the locations of central

1 1

flashes observed by Nicholson *et al.* (1995). The inset of Figure 1.1 shows the 1 bar geoid as calculated based on the zonal wind profile for Saturn (Appendix A). The main figure is the difference between the wind-free geoid and the shape based on zonal winds at the 1 bar level.

Table 1.1 Coordinates and Specifications of Telescope Used in Observations (Olkin 1997).

Telescope	Longitude	Latitude	Altitude	Aperture	Instrument
IRTF	-155° 28' 20" E	19° 49' 34"	4182 m	3.0 m	NSFCAM[1]
					Rochester
					InSb Array[2]

Table Notes:
1. Shure *et al.* 1994.
2. Forrest *et al.* 1990.

Table 1.2 Observed Stellar Occultation Parameters

	28 Sgr	GSC5815-01190	GSC5249-01240
Star Position (J2000.0): α_s	$18^h 46^m 20^s.595$	$22^h 41^m 00^s.965$	$23^h 19^m 34^s.5947$
Star Position (J2000.0): δ_s	$-22^\circ 23' 32".05$	$-10^\circ 28' 19".10$	$6^\circ 47' 10".4411$
Event Observed	Immersion	Emersion	Immersion
Half-light Time of the Event (UTC): $t_{\frac{1}{2}}$	1989 7 03 06 54 58.545	1994 9 18 10 31 23.340	1995 11 20 06 14 46.855

1.3   Occultation Observations

The three stellar occultations for this study were observed at NASA IRTF using the Rochester InSb Array (Forrest *et al.* 1990) in 1989 and NSFCAM (Shure *et al.* 1994) in 1994 and 1995. In Table 1.1 we have listed the coordinates of IRTF. In Table 1.2 we have listed

location in J2000.0 coordinates and event times for each of the three events that occurred in 1989, 1994, and 1995.

1.3.1 28 Sgr

As part of an attempt to observe Saturn's ring structure, the 28 Sgr occultation was observed by Harrington et al. (1989) at NASA IRTF on July 3 1989. The event was first predicted by Taylor (1983), and due to its bright magnitude most major telescopes in viewing area recorded the event. The observers of the occultation event at IRTF were J. Harrington (MIT), W. Forrest and J. Pipher (U. of Rochester).
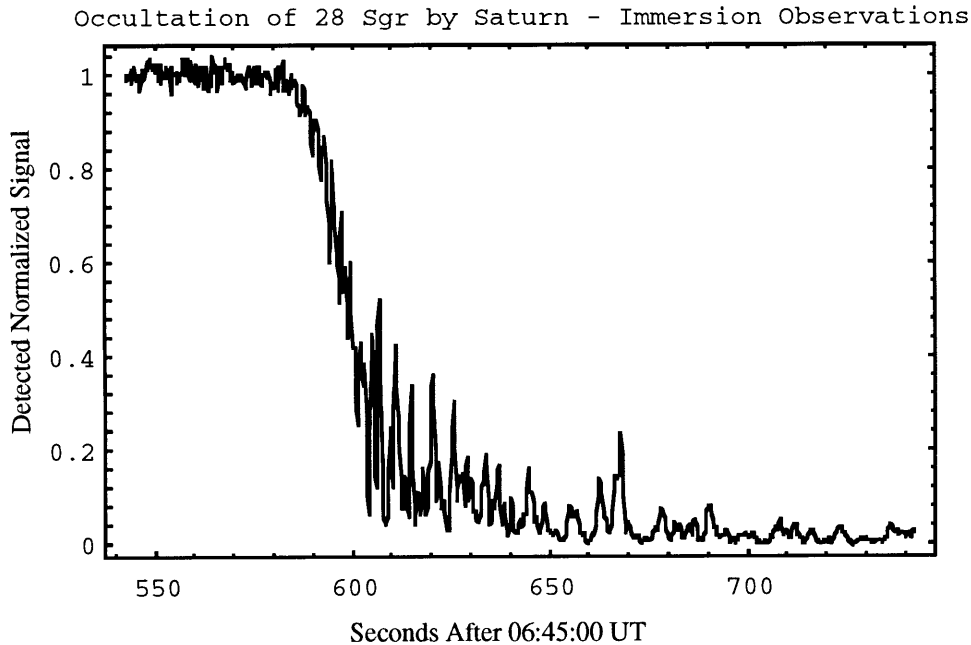
Occultation of 28 Sgr by Saturn - Immersion Observations

Figure 1.3 The normalized stellar intensity recorded during the occultation of 28 Sgr by Saturn. Immersion was observed at IRTF by Harrington *et al.* (1989). The time of signal received is marked in seconds past 06:45 UT on July 3, 1989.

The instrument used was the U. of Rochester 62×58-pixel InSb array (Forrest *et al.* 1990) at a filter wavelength of 3.255 μm corresponding to methane and water ice absorption. This minimized the background light from Saturn and rings, simplifying image processing. As part of the ring event observations, atmospheric immersion was also observed. Summary of the immersion

13

observations are presented in Table 1.4, and the light curve is presented in Figure 1.3. Full analysis of the 28 Sgr ring data could be found in Harrington *et al.* (1989) including a full description of time and astrometric calibrations.

Table 1.3   Instrument and Observational Parameters

Parameter	28 Sgr	GSC5815-01190	GSC5249-01240
Camera	InSb Array	NSFCAM	NSFCAM
Stored Frame Size (pixels)	62×12	48×40	160×56
Pixel Scale (Arcsec pixel^{-1})	0.42	0.27	0.31
Integration Time (sec)	0.25	0.158	0.904
Cycle Time (sec)[1]	0.271	0.165	0.949
Central Wavelength (μm)	3.225	2.260	2.280
Filter Bandwidth FWHM (μm)	0.23	0.05	0.17

Table Notes
1. See section 1.4 for details on time calibration for observations with NSFCAM.

1.3.2   GSC5815-01190

Occultation of GSC5815-01190 (approximate V=11.7) by Saturn was predicted by Bosh and McDonald (1992) and the prediction was later confirmed to determine the possible observable locations with the Shoemaker films at Lowell Observatory. Figure 1.4 shows the predicted path of the star, and the shadow map of the possible observing locations. Since Hawaii happens to be in the middle of this shadow, preparations were made to observe the event there with two telescopes: NASA IRTF and U. of Hawaii 88 inch telescope. The two observations were designed such that IRTF would observe the event in infrared using NSFCAM, and 88 inch telescope would observe in visible using the MIT PCCD. The two light curves in different wavelengths could then be used to derive the hydrogen to helium ratio of Saturn, based on delay in spikes in one wavelength with respect to the other (Elliot *et al.* 1974).
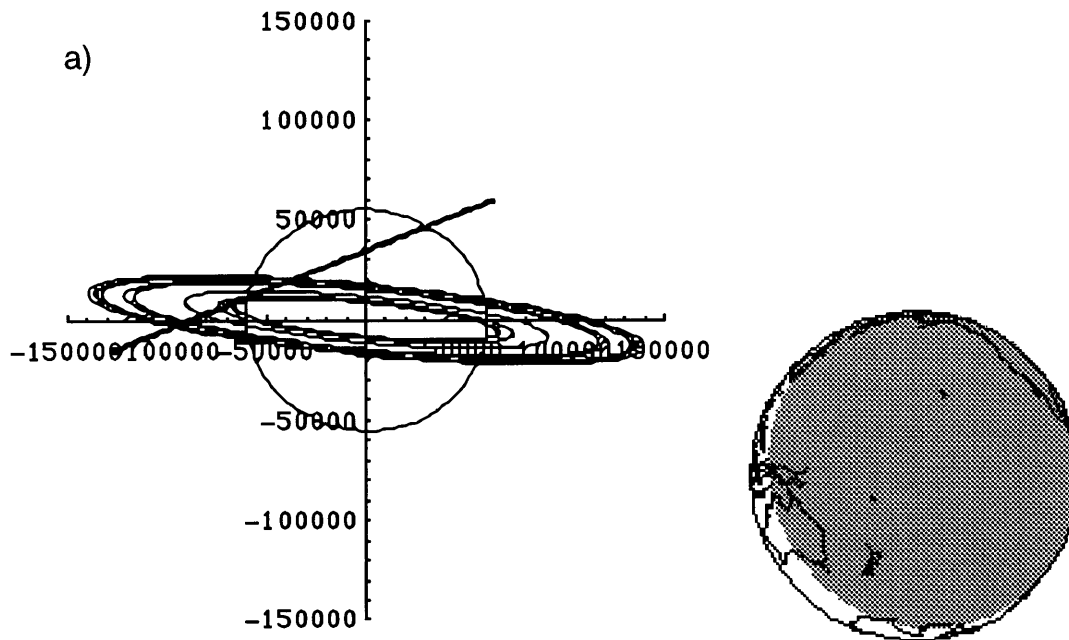
Figure 1.4 a) Apparent path of GSC5815-01190 through Saturn's atmosphere and rings on September 18, 1994. The track was computed based on the ephemeris of Saturn and its satellites. The error in track is mostly due to the error in star position which amounts to ± 2 arcsec. b) The shadow of the GSC5815-01190 occultation This is the globe of Earth as seen from Saturn at the mid time of the occultation. The shaded region indicates where the sun was below −12° altitude. As shown, the occultation was visible from most of the pacific islands and observations were made from Hawaii.

Observers at NASA IRTF were J. Elliot (MIT) and A. Bosh (Lowell Observatory) and at U. of Hawaii 88 inch telescope were H. Hammel and J. Foust (MIT). Bad weather conditions permitted observations only at the NASA IRTF, and only emersion was observed. The same bad conditions allowed the IRTF telescope dome to be opened only a few minutes before the predicted event time. This short time after the clearing didn't allow us to do routine instrument checks, including instrument focusing. In the movie mode of NSFCAM, which is used for time series observations such as occultations, the imaged frames are not displayed until the series has stopped. At the end of our observations, we found that we had not properly focused the instrument. Also the star had moved partially out of the image frame while the event was progressing (Figure 1.5). The full level, after the emersion, in Figure 1.6 shows strong variations in intensity. Based on these intensity changes and the observing conditions, we caution the

15

use of results from this event to study Saturn's atmosphere. The observed high intensity spikes of this occultation may carry important statistical information as to the behavior of Saturn's atmosphere near the equator and can provide valuable data for a subsequent study.
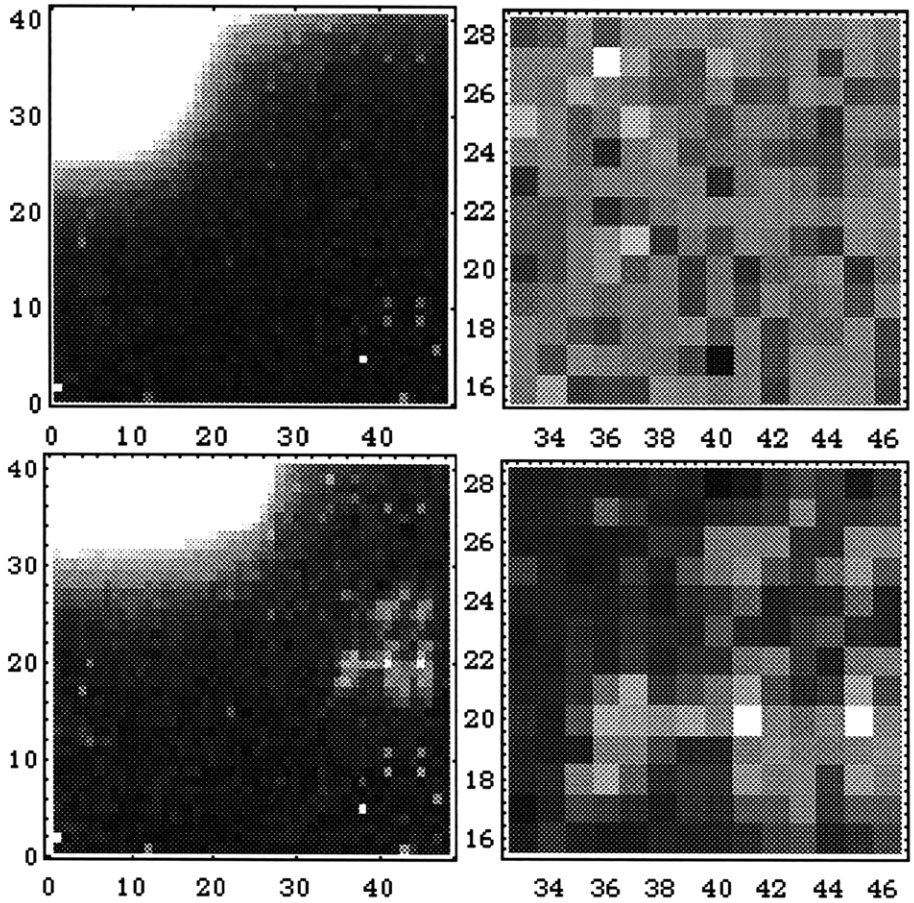

Figure 1.5 Sample images from Saturn occultation of GSC5815-01190. The top panel (frame 40) shows an image before the appearance of the GSC star in images, while the bottom panel (frame 1400) shows the appearance of the unfocused star at the middle of the right-hand side of the frame (between rows 15-25 and columns 32-45). Saturn is the bright object on top left corner of both frames. The data were recorded using the NSFCAM with a K band filter at an integration time of 0.158 seconds. The image scale is approximately 0.3 arcsec pixel[-1]. The frames on the right show a magnified view of the pixels containing the unfocused stellar image.
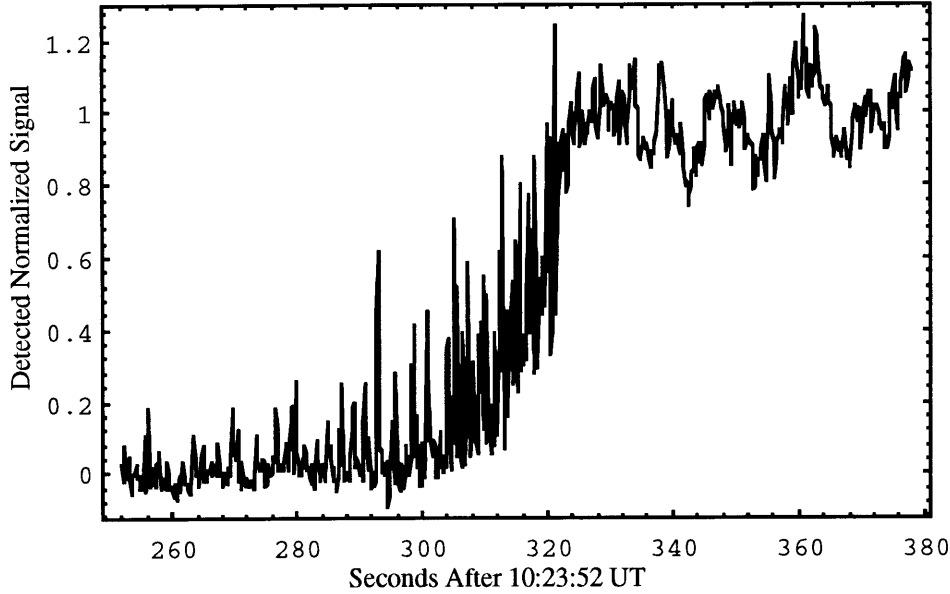
16

Figure 1.6 The normalized stellar intensity recorded during the occultation of GSC5815-01190 by Saturn. Emersion was observed at IRTF using the NSFCAM. The time of signal received is marked in seconds past 10:23:52 UT on September 18, 1994. The observed stellar intensity is normalized for data reduction purposes. The observed intensity spikes in the light curve are primarily due to the density inhomogeneities. The inversion procedure, described in Chapter 3, is used to retrieve the variations based on the amplitude of the observed intensity spikes.

Table 1.4 Occultation Astrometric Parameters

Parameter	28 Sgr	GSC5815-01190	GSC5249-01240
$\langle v_\perp \rangle$ (km sec^{-1})	20.515	19.143	0.586
$f_h - f_0$ (km)	251.3	–11411.5	–910.4
$g_h - g_0$ (km)	–2433.4	29115.3	54901.9
P_s (degrees)	6.25	5.68	5.02
B_s (degrees)	25.40	8.99	2.67
D (AU)	9.021	8.745	9.194
ϕ_h (degrees)	–12.47	2.27	84.45

17

Table 1.5 Saturn Parameters Used in this Study

Parameter	Adopted Numerical Value	Reference
Mass of Saturn (kg)	$5.68598\ 10^{26}$	Lindal et al. 1985
System III Rotation period	10hr 39min 22.4sec	Davies et al. 1983
Equatorial Radius (1 bar level km^{-1})	$60268\ \pm4$	Lindal et al. 1985
Mean Polar Radius (1 bar level km^{-1})	$54364\ \pm10$	Lindal et al. 1985
Oblateness $\varepsilon = \dfrac{R_{eq} - R_p}{R_{eq}}$	$0.09796\ \pm0.00018$	Lindal et al. 1985
Saturn's Zonal Gravity Coefficients - J2	$(16297\pm18)\ 10^{-6}$	Nicholson and Porco 1988
Saturn's Zonal Gravity Coefficients - J4	$(-910\pm61)\ 10^{-6}$	Nicholson and Porco 1988
Saturn's Zonal Gravity Coefficients - J6	$(-107\pm50)\ 10^{-6}$	Nicholson and Porco 1988
Saturn's Pole Position (J2000.0, at Voyager I epoch of UTC 1980 Nov. 12 23:46:32): α_p	$40°.5929\pm0.°0151$	Elliot *et al.* 1993
Saturn's Pole Position (J2000.0, at Voyager I epoch of UTC 1980 Nov. 12 23:46:32): δ_p	$83°.5348\pm0.°0053$	Elliot et al. 1993
$\dfrac{d\alpha_p}{dt}4$(deg yr^{-1}, J2000.0)	-0.00061172	Elliot et al. 1993
$\dfrac{d\delta_p}{dt}4$(deg yr^{-1}, J2000.0)	-0.00006420	Elliot et al. 1993

1.3.3   GSC5249-01240

Saturn and its rings occulted star GSC5249-01240 on November 20-21, 1995. The star was one of the brighter candidates identified by Bosh and McDonald (1992) in a search program to find possible Saturn stellar occultations from the Guide Star Catalog (STScI 1989; Jenkner *et al.* 1990; Lasker *et al.* 1990; Russell *et al.* 1990): V=11.9 and K=10.6. During infrared photometry of this star, a companion approximately 2 magnitudes fainter at K and 2 arcsec away was found. This star was also identified in the search as one with the slowest velocity of 0.58 km sec^{-1}, and to be occurring at the time of Saturn's ring plane crossing. Figure 1.7 shows the apparent path of the primary star during the occultation, whereas Figure 1.8 shows a series of images.
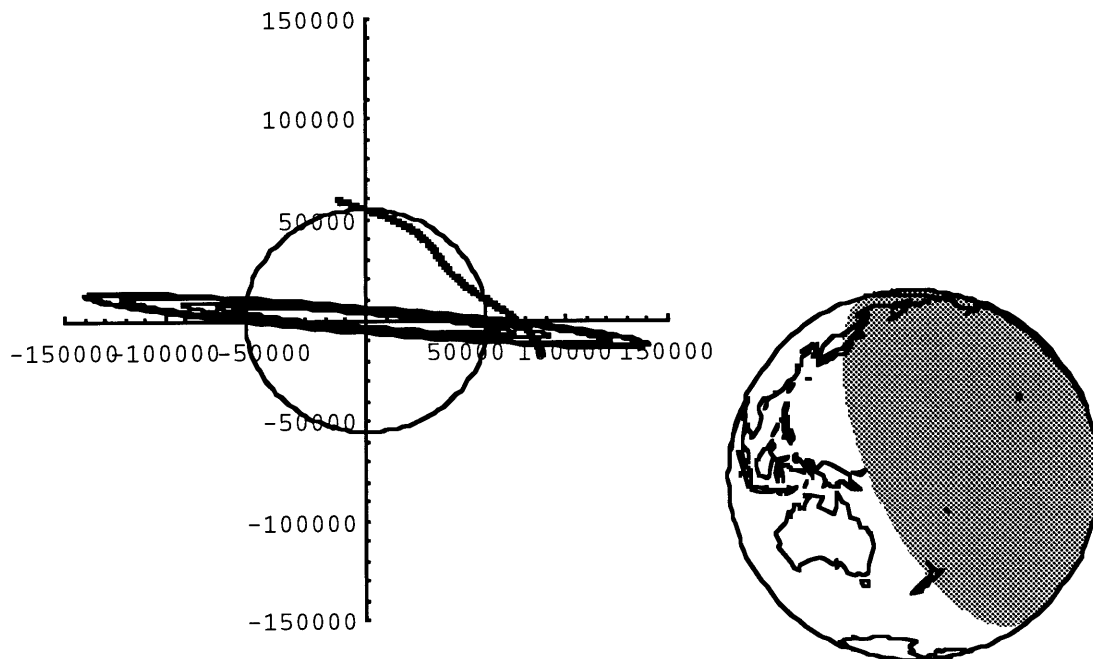

Figure 1.7   a) Path of GSC5249-01240 through Saturn's atmosphere and system on November 20-21 1995. The track was computed from the times of ring events observed during the ring occultation. b) The shadow of the GSC5249-01240 occultation. This is the globe of Earth as seen from Saturn at the mid time of the occultation. The shaded region indicates where the sun is below 12° altitude. As shown, the occultation was visible from most of the Pacific islands and observations were made at Hawaii.

Occultations with low velocities have the advantage that a high spatial resolution, as low as 1 km, at Saturn can be easily achieved with typical integration times used for occultation observations with modern high speed cameras. Given that the other successful occultation observations occurred at velocities of 15 to 20 km sec^{-1}, this would then give an event with a total integration time 15 to 20 higher than before, thus increasing the single-to-noise ratio per km of distance probed by at least 6 times for a star of same magnitude.
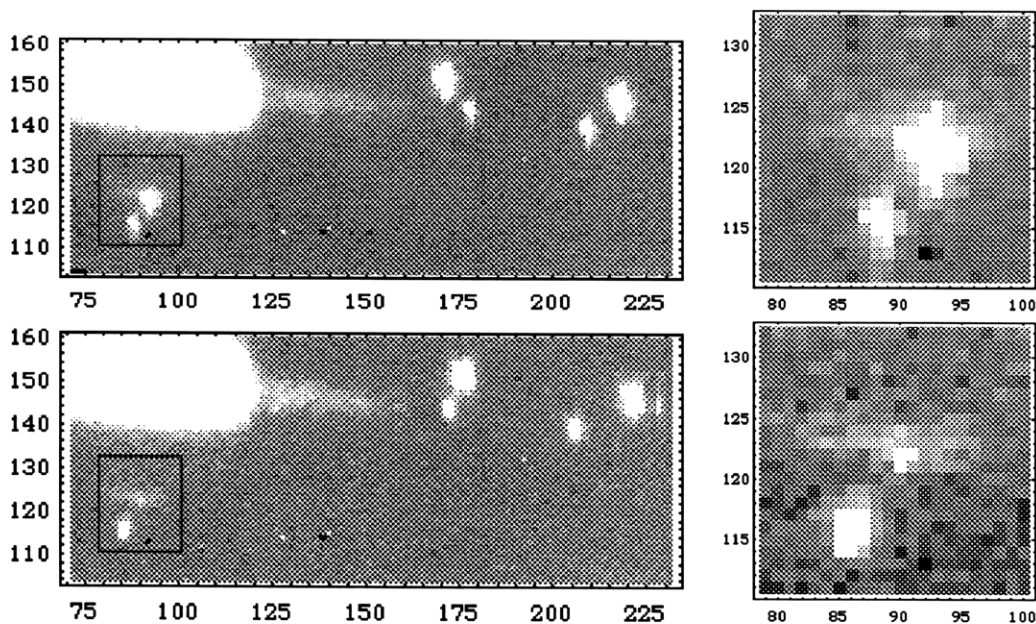
Figure 1.8 Data Frame of Saturn System on Nov. 20 UT before (top panel) and during the Saturn Occultation of GSC5249-01240. The data were recorded using the NSFCAM with "Spencer 2.3" filter. North is down, east is to the right. Several Saturnian satellites are visible on the right side of the frame The two stars, GSC5249-01240 and its companion (K=12.6) is on the northern hemisphere of Saturn and the bright star is occulted. Note that the entire northern hemisphere is invisible, except for few haze features.

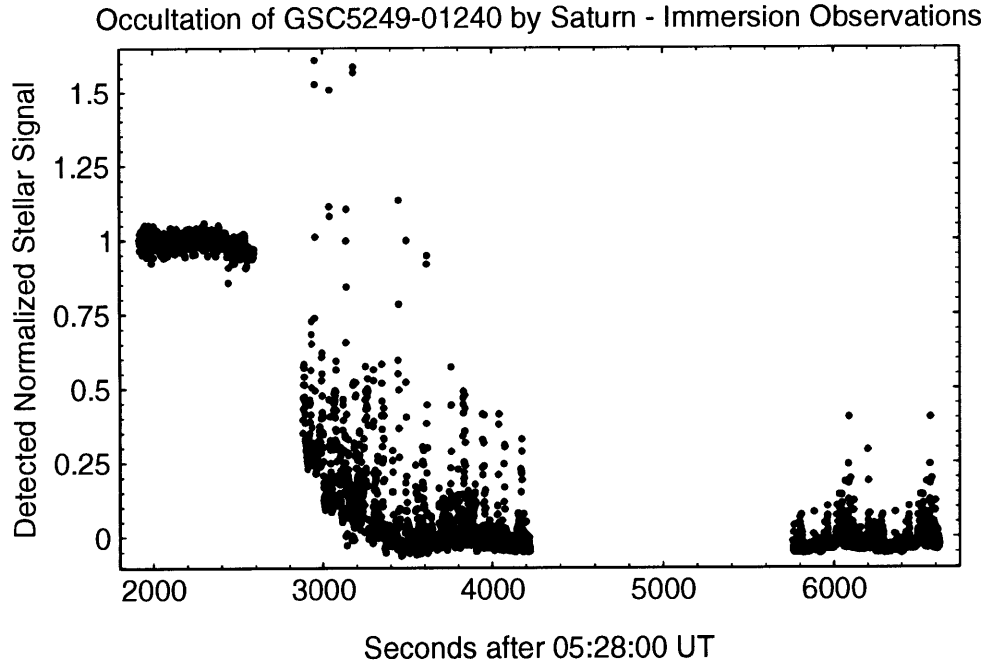Occultation of GSC5249-01240 by Saturn - Immersion Observations

Figure 1.9 The normalized stellar intensity recorded during the occultation of GSC5249-01240 by Saturn. Immersion was observed at IRTF using the NSFCAM. The time of signal received is marked in seconds past 05:28 UT on November 20, 1995.

1.4 LED Calibration Tests

NSFCAM records an accurate GPS time (which is written in the FITS header) only at the beginning of the observation. After that, the integration time is controlled by the internal PC clock, which is not necessarily accurate. If the PC clock is fast or slow, the offset to the integration time will accumulate over the course of the multi-frame observation and can add up to a very significant deviation between the presumed time, based on the PC clock, and the real UT time. Additionally, there is a delay between the recording of the GPS time and the start of the first frame integration, referred to as the initialization delay time. For each configuration we need to establish the dead time between integrations and the initialization delay, as it depends on the number of pixels being read out and the location of those pixels. Smith (1995) contains a full description of time calibration for the NSFCAM based on data obtained during the 1994 occultation observation run.

In order to establish the dead time and initialization delay we recorded a series of sub frames in the same configuration as the occultation observations (box size, box location, integration time and series length) looking at a blinking infrared LED. This LED was illuminated at regular one second intervals by triggering it with the Trak Systems' GPS 1 PPS precision square wave. The timing analysis was applied to 1995 November 20 data collected at an integration time of 0.904 seconds. To establish the dead time, The LED was triggered by the 1 Hz output of a GPS receiver. The first 48 images from the series is displayed in Figure 1.10. Because the exposure time was 0.904 sec, the LED is initially seen in every other image. As the LED is triggered at 1 Hz the difference between the one second and the presumed integration time is the offset introduced in the LED series.

The number of LED frames between transitions from illumination to dark, N_t, is related to the offset to the support integration time, ε, based on following equation (Smith 1995 and Roberge 1996),

$$N_t(96ms - \varepsilon) = 904ms + \varepsilon = T_f \qquad (1.1)$$

where T_f is the real integration time. The results from the analysis is tabulated in Table 1.6.

Recently Olkin (personal communication) informed that the modeling of the subsequent ring occultation times suggest a deadtime of 43 msec for the November 1995 GSC5249-01240 occultation data. The derivation of this value is to be included in a paper to be published on the ring occultation observations and modeling (Bosh et al., in preparation). We have opted to use the 43 msec value given that we have already used the information from the ring timings to create the star path during the atmospheric occultation. It is not yet clear why the two methods give two different values for the deadtime. But the error of 2 msec between the two timing methods, only produces an error of roughly 4 km in the half-light radius. As shown in Chapter 2 this is less that the error due to model fits.

Table 1.6: Results of LED calibration analysis for GSC5815-01190 and GSC5249-01240 occultation data.

	1994 GSC5815-01190 $T_i = 0.250$ sec	1995 GSC5249-01240 $T_i = 0.904$ sec
Number of frames between transitions, N_t	609.0 ± 0.20	18.80 ± 0.05
Offset to integration time, ε	0.40 ± 0.01 ms	43 ms
Real integration time, T_f	249.59 ± 0.01 ms	947 ms
Initialization delay, t_{id}	13.62 ± 0.41 ms	0.781 ± 0.013 sec

23.53.1701.1.fits   Frames 1-48

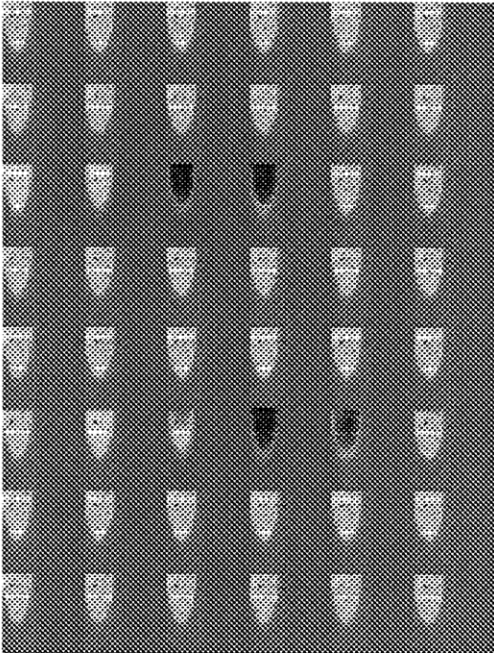**Figure 1.10** The first 48 images in the LED calibration series, from left to right. The image series was used to establish the dead time in the readout of the array. The LED was triggered by the 1 pulse sec^{-1} (triggered by a GPS receiver). The exposure time for each image is 0.904 seconds. The alternating pattern of the LED on and off can be seen. Also evident is the transition of this pattern due to the dead time.

Chapter 2
Isothermal and Thermal-Gradient Model Fits

2.1 Introduction

In this chapter we have described our analytical model fitting procedures for retrieving basic data on Saturn's atmosphere. An alternative method, the inversion method, is described in the next chapter. For a giant planet like Saturn where intensity spikes dominate the light curve, isothermal and power-law thermal gradient model fitting is not the ideal method to derive the structure parameters. As an initial modeling procedure, here we make isothermal model fits to set the half-light radius level, from the center of Saturn, when the light has either dropped or increased to half of the full level. Finally a temperature gradient model is fit to the data to test for any evidence for deviations from isothermal behavior.

2.2 Method

We used the same methods as developed by Elliot and Young (1992; hereafter EY92) to model the light curves and thereby derive important structural parameters, such as temperature and pressure. The procedure derived by EY92 was to derive the atmospheric structure of a small planet, Pluto, where rotational term does not contribute significantly to the gravitational acceleration. But in the case of large planets, the rotational term needs to be considered in the analysis. According to current models based on spacecraft data, the atmosphere of Saturn is not isothermal. The results from this analysis should be used only for comparative purposes with results from similar studies, such as the analysis of 14 light curves observed during the 28 Sgr occultation of July 3 1989 by H97. Despite the limitation that isothermal atmosphere deviates from the true

atmosphere, isothermal fits provide vital information including initial conditions for the inversion algorithms used in the next chapter.
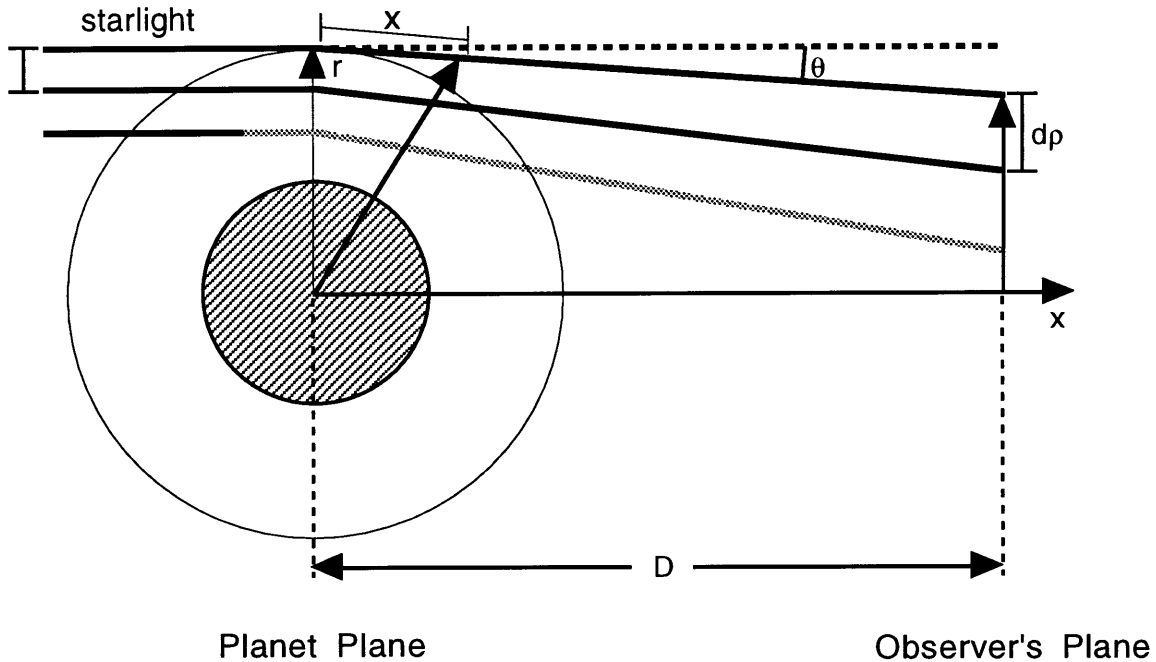

Figure 2.1. Stellar occultation by a planetary atmosphere. Starlight encounters a planetary atmosphere and is bent by refractivity in the atmosphere. Since the refraction increases exponentially with depth in the atmosphere, two neighboring rays separate by an amount proportional to distance from the planet, which causes the star to dim as seen by a distant observer. Other dimming effect is atmospheric extinction due to absorption and scattering. In the case of Saturn, starlight is also bent due to general relativistic effects. Figure is reproduced from Elliot and Young (1992).

The basic process can be described using Figure 2.1. Parallel rays of monochromatic starlight are incident on Saturn's atmosphere from the left. The observer's plane (also defined as the shadow plane), perpendicular to the incident light rays—which are aligned with the x-axis, is located at a distance D from the center of Saturn. The coordinate r is the radius in the planet plane as measured from the center of Saturn. Starlight with a closest approach to the planet r is bent by the refraction angle $\theta(r)$, measured negative toward the

25

planet. At any point in Saturn's atmosphere, the light ray is a distance r' from the center of the plane where,

$$r'^2 = r^2 + x^2. \tag{2.1}$$

The stellar flux, upon passing through Saturn's atmosphere, will be changed by three effects: (1) differential bending of the light rays, (2) extinction (either by absorption and/or scattering by the atmosphere), and (3) partial focusing of the light by the curvature of the planetary limb in the plane perpendicular to ray path. From the analysis of EY92 we can consider these three effects and write the flux received by the observer, $\varsigma(r)$, as:

$$\varsigma(r) = \frac{r}{\rho(r)} \left| \frac{dr}{d\rho(r)} \right| \exp[-\tau_{obs}(r)], \tag{2.2}$$

where τ_{obs} is the line-of-sight optical depth and $\rho(r)$ is the shadow-plane radius. Based on the distance to Saturn, D, the shadow-plane radius can be written as:

$$\rho(r) = |r + D\theta(r)|. \tag{2.3}$$

Taking the derivative we can write the focusing term as (EY92 equation 2.3):

$$\left| \frac{dr}{d\rho(r)} \right| = \frac{1}{\left| 1 + D\frac{d\theta(r)}{dr} \right|}. \tag{2.4}$$

The total bending of the ray is the integral of the curvature over its path. For an elliptical planet like Saturn, this bending is determined by the radius of curvature instead of radius itself. Therefore it is necessary that the focusing term in equation 2.2 be rewritten in terms of the line of sight radius of curvature. Other than differential bending, an additional bending is also introduced due to the general relativistic effects. At this stage we ignore the general relativistic bending, but later we correct our radii values by adding the necessary contribution.

26

We can write the refraction angle using the refractivity $v(r)$ as:

$$\theta(r) = \frac{d}{dr}\int_{-\infty}^{+\infty} v[r'(x,r)] = \int_{-\infty}^{+\infty} \frac{\partial v[r'(x,r)]}{\partial r}dx = \int_{-\infty}^{+\infty} \frac{r}{r'}\frac{dv(r')}{dr'}dx. \qquad (2.5)$$

In our subsequent analysis we will ignore the extinction effects, either due to absorption processes and/or scattering due to particles in the atmosphere. Later, based on our model fitting results and other studies on haze observations in the upper atmosphere, we will investigate the existence of haze in the altitude region probed by our occultations. Since none of our data included central flash observations, we will not address such issues here.

Our isothermal model fits to the observed light curves were based on the derivation by EY92. We have slightly modified some of the equations in their study to account for the significant rotational contribution due to centrifugal term in Saturn. For example, we can write the change in pressure across the atmosphere, $dp(r)$, based on hydrostatic equilibrium as both due to gravity and rotation as:

$$dp(r) = -g(r)\mu m_{amu} n(r) dr \qquad (2.6)$$

where $g(r)$ is the gravitational acceleration value calculated based on the Appendix A, μ is the mean molecular weight, m_{amu} is the mass of one atomic mass unit and $n(r)$ is the number density of the atmosphere at radius r.

We can write the pressure scale height at the reference radius as simply:

$$H_h = \frac{r_h}{\lambda_{g0} - 2\lambda_{\omega 0}}. \qquad (2.7)$$

where λ_{g0} and $\lambda_{\omega 0}$ are the contributions due to gravitational and rotational terms (see EY92). We refer reader to the EY92 for most of the other equations that relate pressure to number density and temperature which were used in this study for derivation of structure parameters based on model fit. The only difference between this work and EY92 is that we have carried through out the

rotational contribution, where as EY92 ignores it, as it was unnecessary for their Pluto analysis.

We determined the half-light radius based on the (f,g) coordinate system as formulated by Elliot *et al.* (1993). The astrometric information used is listed in Table 1. The position of the IRTF relative to the center of the Saturn was solved based on a solution of the ring occultation by Bosh and Olkin (1996) and was used to compute the f and g values along the path of the star, as described earlier. With these (f,g) values we wrote our flux values as a function of radius, rather than time, and made isothermal fits to the normalized signal vs. radius. This fitting procedure was used to determine the full level, the background level, ρ_h and λ_{gh}.

The parameter ρ_h determines the half-light radius in the shadow plane. This is the geometric radius of the half-light level, which can be written as:

$$\rho_h = \left[(f_h - f_0)^2 + (g_h - g_0)^2\right]^{\frac{1}{2}}, \tag{2.8}$$

where we have evaluated $f(t)$ and $g(t)$ at the time of half-light $(t = t_h)$:

$$f_h \equiv f(t_h) \quad \text{and} \quad g_h \equiv g(t_h). \tag{2.9}$$

In equation 2.8 f_0 and g_0 represent the fg component values for the ephemeris correction determined from fit to the ring occultation observations (See Elliot *et al.* 1993, pg. 2560).

The same calculation can be done by transforming the (f,g) coordinate system in the shadow plane to (u,v) coordinate system in the body plane based on the formulation by Elliot *et al.* (1993). If measured in the two planes, shadow and body, the two half-light radii differ by an amount equivalent to the scale height of the planetary atmosphere (H_h) and the deflection due to general relativity (Δr_{grav}). The first term is due to the refractive bending of the half-light ray from planet plane to the observer plane. The amount due to general relativistic deflection can be written as:

$$\Delta r_{grav} = \frac{4GM_s D}{rc^2}, \tag{2.10}$$

where c is the speed of light and D is the distance to Saturn at the time of observations. For an oblate planet like Saturn, the minimum light level probed does not lie in the plane of the sky but at a planet either behind or front by a small amount. This is a geometric correction that was first included by Baron *et al.* (1989) in the derivation of oblateness of Uranus. Thus, with the general relativistic, refraction, and geometrical correction the half-light radius can be written as:

$$r_h = \left(\rho_h + \Delta r_{grav} + H_h\right)\left[1 + \gamma^2 \frac{\sin^2 \phi_h}{\cos^2 B_s}\right], \tag{2.11}$$

where ϕ_h is the planetocentric sub-occultation latitude at the half-light level determined based on the position angle of the pole P_s, and sub-Earth latitude B_s (Elliot *et al.* 1993). In equation 2.11 the factor γ defines the line of projection geometry of Saturn's shape through:

$$\gamma = \frac{-\varepsilon\left(1 - \frac{\varepsilon}{2}\right)\sin 2B_s}{1 - \varepsilon(2 - \varepsilon)\cos^2 B_s}. \tag{2.12}$$

Here ε is the oblateness of the planet given simply as:

$$\varepsilon = \frac{R_{eq} - R_p}{R_{eq}}, \tag{2.13}$$

where R_{eq} and R_p are the equatorial and polar radius respectively. At the 1 bar level the oblateness is 0.098 ± 0.001 (Lindal *et al.* 1985). We have this value in our analysis at the microbar region of the planet.

At the half-light level we can write refractivity as:

$$v_h = \frac{H_h^{\frac{3}{2}}}{D\sqrt{2\pi r_{ch}}} \tag{2.14}$$

where we have included the radius of curvature at the half-light level, r_{ch}, instead of the half-light radius. In the above equation D is the distance to Saturn at the time of observations and H_h is the pressure scale height at the half-light radius. The radius of curvature

here is defined in the plane containing the center of the planet and the line of sight. Based on the geometry, the three dimensional Saturn can be projected into a two dimensional ellipse and the radius of curvature can be evaluated based on the elliptical shape of Saturn. Alternatively one can use the knowledge of location of each of the rays and calculate the phase shift based on the path traveled by the ray. For more information on the alternative method for derivation of the path traveled by each of the light rays please see H97. The radius of curvature instead of the radius changes the scale height at the constant refractivity level by about 3 to 4% depending on the latitude.

Infrared data acquired with the Pioneer 11 spacecraft indicated that Saturn's atmosphere consists of 90 ± 3% of hydrogen and 10 ±3% of helium by number density, which corresponds to a molecular mass of 2.215 ± 0.060 amu (Orton and Ingersoll 1980). Subsequent measurements with Voyager has shown a hydrogen abundance of 94% (Lindal *et al.* 1985). Conrath *et al.* (1984) has interpreted the spacecraft data with an atmospheric model of 96.3% H_2, 3.3% He, and 0.4% CH4 with a molecular mass of 2.136. For the purpose of our analysis we have adopted a hydrogen abundance of 94 ± 3%; the remainder is assumed to be primarily helium. The mean molecular mass of this mixture is 2.135 amu with an uncertainty of about 2.5%. At standard temperature and pressure this gas mixture corresponds to a refractivity, v_{STP}, of 1.30×10^{-4} (Elliot *et al.* 1974) at the wavelength of our observations.

Based on the values for molecular weight, refractivity at standard temperature and pressure and refractivity at the half-light level, we can write the number density at the half-light level as:

$$n_h = \frac{N_L v_h}{v_{STP}},$$
(2.15)

where N_L is the Loschmidt's number. Using the number density at the half-light level we can write the pressure at the half-level as:

$$p_h = n_h k T_h,$$
(2.16)

where T_h is the isothermal temperature of Saturn. The isothermal temperature of a planet is related to the scale height, H_h, and local acceleration of gravity, g, through:

$$T_h = \frac{H_h \mu m_{amu} g}{k} .$$ (2.17)

In Table 2.1 we have derived the atmospheric quantities based on the values obtained for r_h and λ_{gh} through isothermal fits (Table 2.1) and the knowledge of gravity as described in Appendix A.

2.3 Thermal-Gradient Model Fits

In Section 2.2 temperatures were derived from isothermal fits to the entire light curves, corresponding to several scale heights, with possible temperature gradients over the altitude range probed by the occultation. The fits to noisy or spiky data cannot differentiate between an isothermal and a nonisothermal profile simply based on fits (Wasserman and Veverka 1973). Fitting with models including temperature gradients could certainly improve the possibility of detecting a nonisothermal atmosphere (EY92). The EY92 thermal gradient model assumes that the temperature follows a power law of the form:

$$T(r) = T_0 \left(\frac{r}{r_0} \right)^b .$$ (2.18)

The power-law index is related to the temperature gradient through the following equation:

$$\left. \frac{dT(r)}{dr} \right|_{r=r_0} = \frac{bT_0}{r_0} .$$ (2.19)

At the halflight radius of the 1994 occultation, the power-law index translates to a temperature gradient of -0.389 ± 0.076. This value supports a possible thermal gradient in the atmosphere probed but due to the additional problems associated with data we are reluctant to conclude this possibility.

The 1994 event was plagued by bad observing conditions (high humidity and clouds), which cleared just before the event so there was no time to carefully focus the telescope. Due to the errors with tracking, the star moved out of the frame as the event progressed and

the existence of a thin haze in the Earth's atmosphere may have changed the refractive properties of the atmosphere, contributing to the observed temperature gradient.
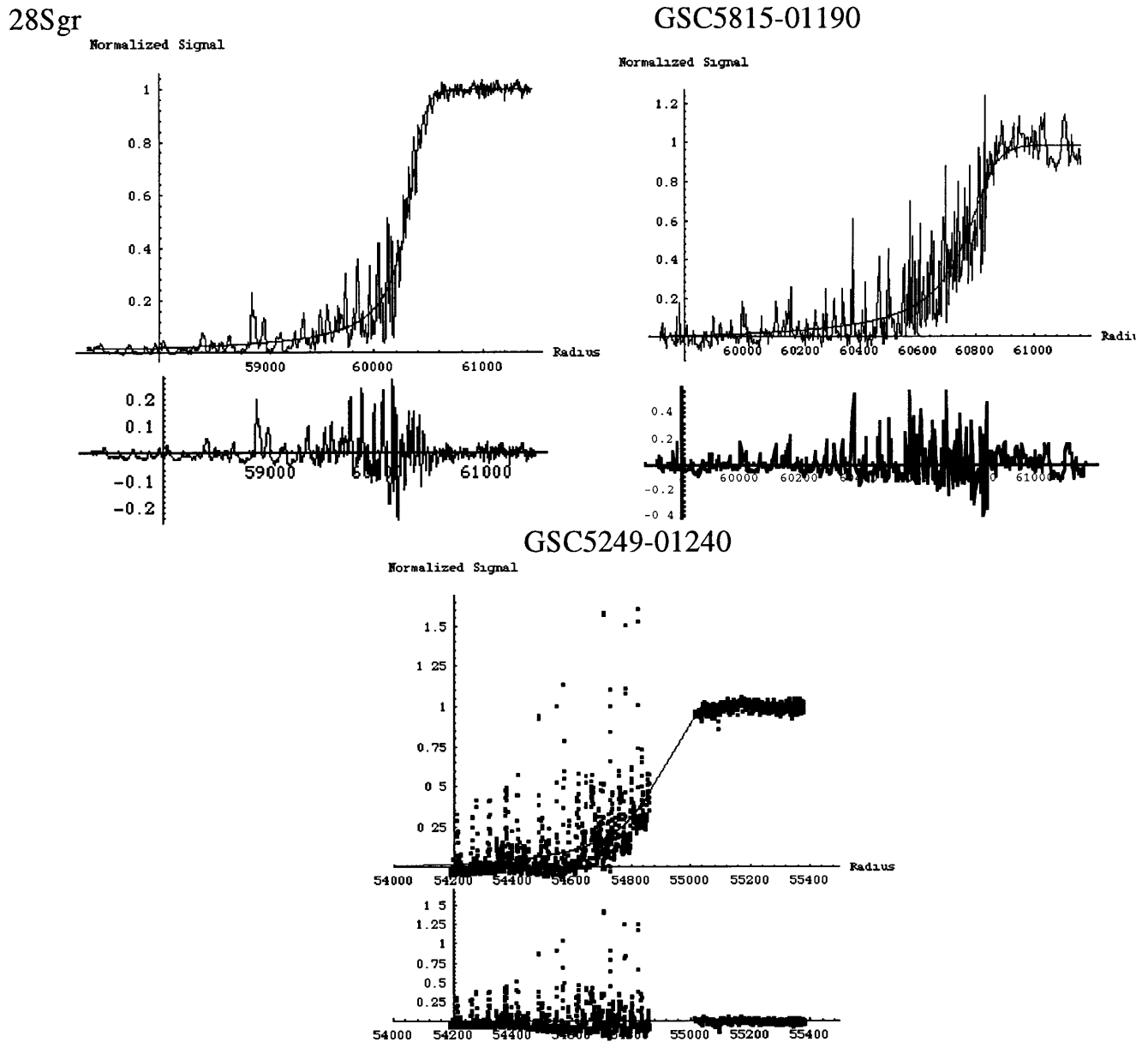

Figure 2.2. 28 Sgr, GSC5815-01190, GSC5249-1240 light curve data, models, and residuals. For the 28 Sgr and GSC5249-01240 events the isothermal model had half-light radius, energy level, full level and background level as variables whereas for the GSC5815-01190 event the half-light level was fixed based on the value expected for an event at the latitude of Saturn.

2.4 Discussion

Table 2.1 Parameters derived from isothermal model fits

Parameter	GSC5815-01190	GSC5249-01240
Background Level	-0.034 ± 0.009	-0.038 ± 0.009
Full Level	0.984 ± 0.006	1.003 ± 0.006
ρ_h (km)	60792.8 ± 4.1	54909.4 ± 8.2
H_h (km)	43.04 ± 2.47	44.3 ± 4.3
Δr_{grav} (km)	36.8	41.5
γ	-0.022	-0.011
r_h (km)	60863.7 ± 5.5	54959.3 ± 9.7
λ_h	1402 ± 118	1239 ± 121
g (cm sec^{-2})	889.62	1208.54
T_h (K)	109.5 ± 5.6	137.46 ± 10.55
P_h (μ bar)	0.98 ± 0.06	1.54 ± 0.09
n_h (cm^{-3})	$(7.20 \pm 0.06) \times 10^{13}$	$(7.53 \pm 0.08) \times 10^{13}$

Based on our model fits and after making the above described corrections for general relativistic effect, refractive bending and geometric corrections we find the half-light intensity level to occur at a radius of 54959 ± 10 km. The corresponding energy ratio for the isothermal fit is 1239 ± 120 (Table 2.1). The scale height at this level is 44.3 ± 4.3 km, corresponding to an isothermal temperature of 137 ± 11 K, based on gravitational acceleration value of 1208.5 cm sec^{-2}. The gravitational acceleration value was calculated through the knowledge of rotation and zonal winds as described in Appendix A of Lindal *et al.* (1985). This radius value, at the half-light intensity level, corresponds to a pressure level of 1.54 ± 0.10 μbar, with a number density of $(7.54 \pm 1.10) \times 10^{13}$ cm^{-3}. Also shown in Table 2.1 are the values obtained for out isothermal fits to the GSC5815-01190 emersion observation. The energy-ratio value from the isothermal fits to the GSC5815-01190 emersion observation is 1402 ± 118, which is high for Saturn's atmosphere. We find this may be due to a loss of signal recorded during the observations. We have attributed this to

the movement of star partially out of frame as the observations were done without focusing under minimal weather conditions. A possible thin cloud in Earth's atmosphere may have also contributed to the loss of signal.

Based on isothermal fits to the 28 Sgr occultation observations in 1989, H97 found a mean equatorial temperature of 141±3 K, with a scale height of 62.3±4.8 km. Our model fits for the GSC5249-01240 suggest a temperature of 137±11 K at higher latitudes. These two values suggest an apparent agreement between the temperatures of north polar and equatorial regions of Saturn.

The three occultations under this study provide probes of Saturn's atmosphere at different times from each other. Between the 28 Sgr and GSC5815-01190 events 5 years have past and they provide a baseline to look for seasonal changes in the temperature structure. The GSC5249-01240 event occurred at a latitude of 84.4 degrees on Saturn and provides an observation to compute the temperature gradient between equator and higher latitudes at the microbar region of the upper atmosphere.

The large-scale temporal asymmetries in the upper troposphere and in the stratosphere observed in both hemispheres have been successfully interpreted in the framework of seasonal radiative models by Bezard et al. (1984) and Bezard and Gautier (1985). At the 150 mbar level, an increase in temperature of about 8K at a latitude of 25° was discovered, and was interpreted as due to the 27° obliquity of Saturn. The response of the upper troposphere has been examined by Hanel et al. (1982) in terms steady-state functions, where insolation and atmospheric responses are periodic functions of the orbital period T_0. An important parameter in such calculations is $\Omega_s \tau$, where Ω_s is the seasonal frequency, $\dfrac{2\pi}{T_0}$, and τ is the radiative relaxation time constant, which gives a measure of the thermal inertia of the atmosphere. Its magnitude and phase determine the time dependent components of the temperature. To a first approximation the phase lag of the thermal response to the solar forcing is given by $\tan^{-1} \Omega_s \tau$, and the amplitude of the response is proportional to $\left(1 + \Omega_s^2 \tau^2\right)^{-\frac{1}{2}}$. Estimates of τ based on the scaling appropriate to Saturn by Conrath and Pirraglia (1983) indicate an atmospheric time lag of approximately one sixth of a Saturn year or 5 to 7 terrestrial years.
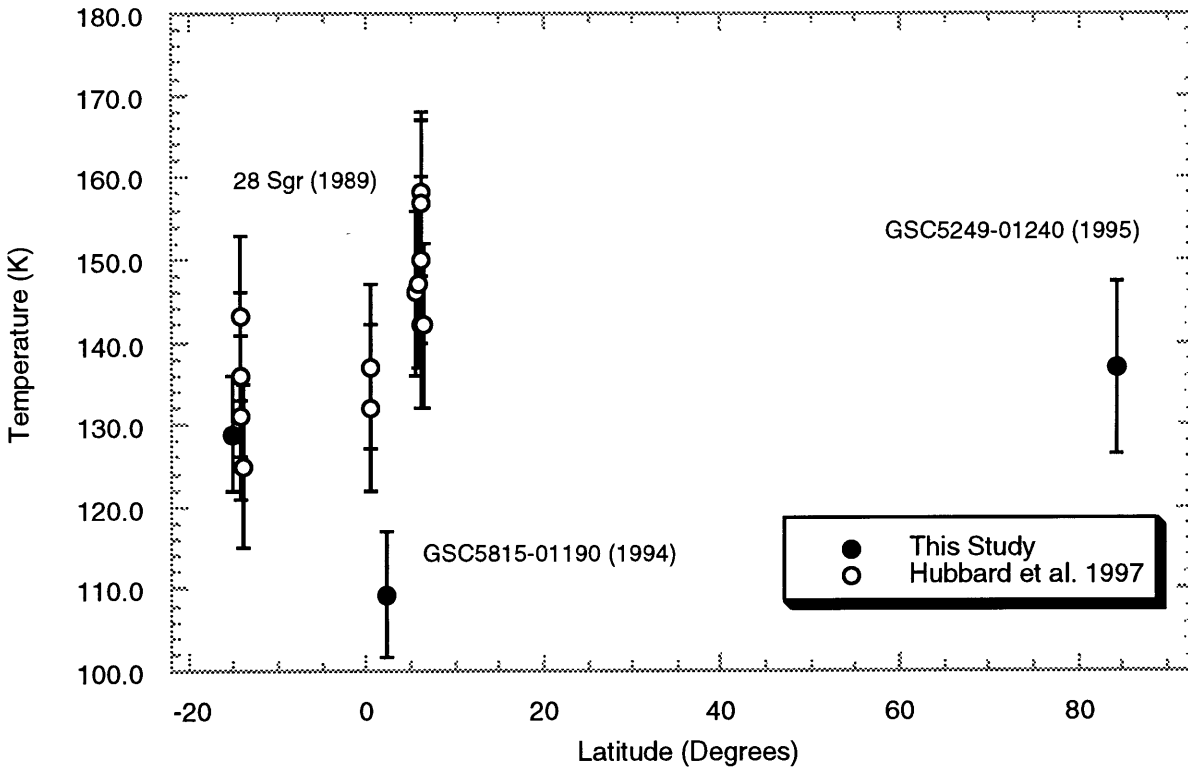
Figure 2.3 Isothermal temperature at the half-light radius vs. the latitude of the sub-occultation point. We find no strong variation in temperature obtained with isothermal fits vs. latitude in Saturn at pressure levels close to 1 μbar.

A radiative seasonal model based on a multilayer transfer treatment has been applied to Saturn's stratosphere by Bezard and Gautier (1985). Figure 2.4 reproduced from their work illustrates the seasonal cycle of the stratospheric north polar, south polar, and equatorial temperatures at pressure level of 5 mbar. Maximum north-to-equator gradients (about 20K) occurred just prior to the Voyager encounters.
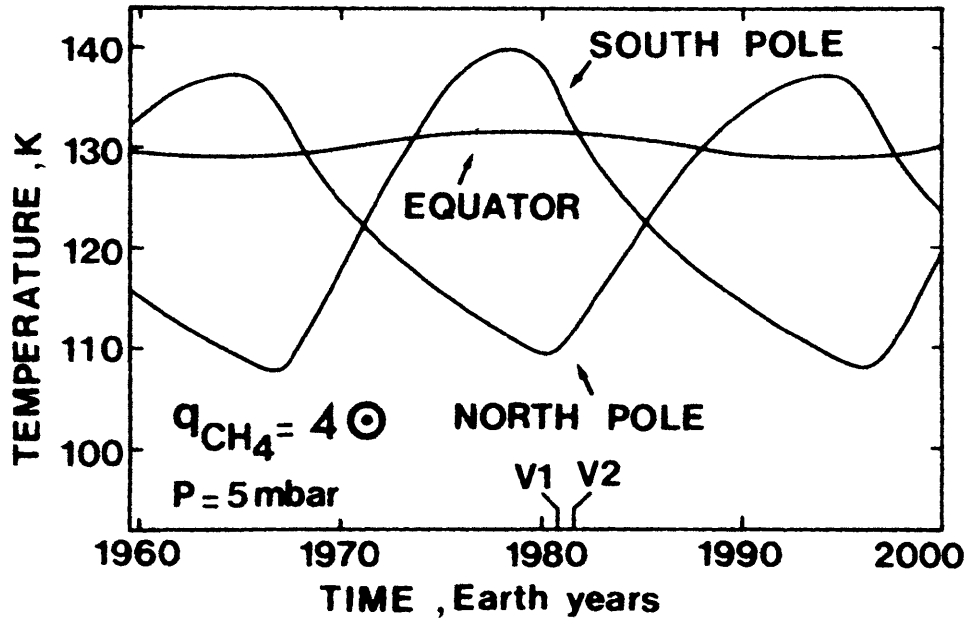
Figure 2.4 Time variation of polar and equatorial temperatures at a pressure level of 5mbar. For comparative purposes Voyager I and II encounter times are indicted. Observations used in this study were obtained near the equator in 1989 and 1994 and near the north pole in 1995. Figure is reproduced from Bezard and Gautier (1985).

Based on this model (Figure 2.4), the equatorial temperature changed only by 5 ± 2 K between 1989 and 1994, where as the difference between north polar and equatorial temperature in 1994-1995 is roughly 8 ± 2 K. In 1989 the temperature difference between equator and north pole was less than 3 ± 2 K. This difference can provide the gradient expected at a higher pressure level than predicted by the theory. Though just one observation may not establish the equatorial-north polar temperature gradient, the light curves obtained by Amanda Bosh with HST should provide more information on latitudinal variation of temperature, pressure and scale height.

In order to test the exact nature of the temperature gradient in the 1994 light curve, we made isothermal fits to the top and bottom half of the light curve separately. The values obtained with separate fits to the top, bottom and full 1994 GSC5815-01190 light curve are tabulated in Table 2.2, and derived quantities in Table 2.3. From these values we find that the top half of the 1994 light curve is in disagreement with the general results found for Saturn. The energy ratio as calculated from isothermal model fits to the top half is

1828±189 where as for the bottom half is 1391±168. This difference propagates through the model fits and produces temperatures at the half-light level of 87.74±6.95 and 115.27±12.00 respectively.
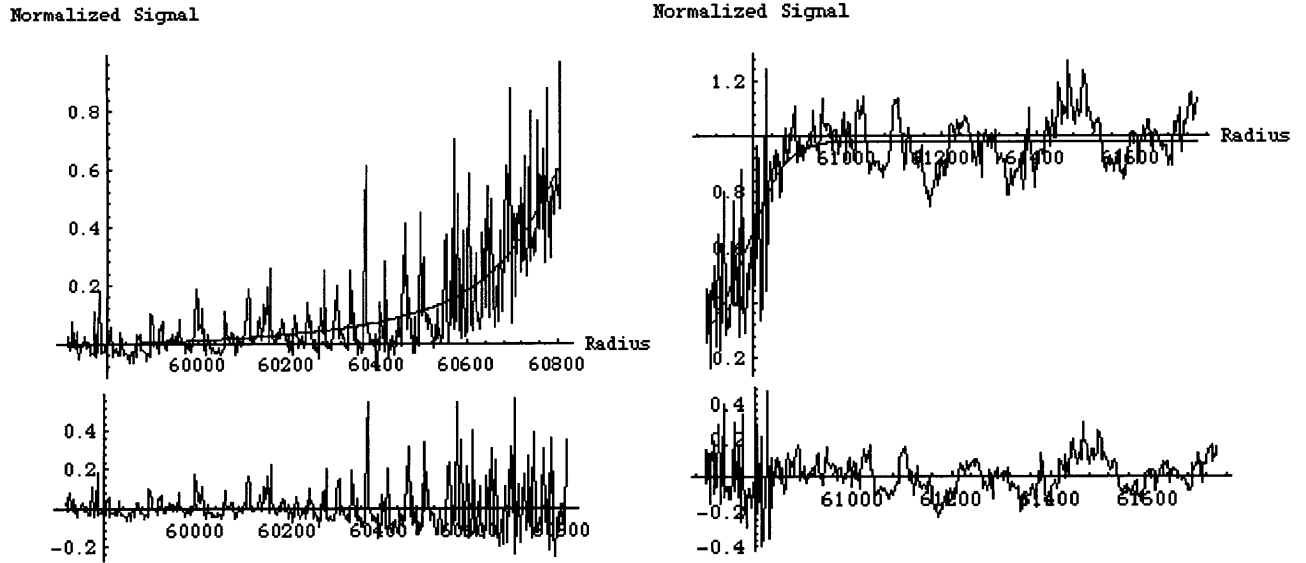

Figure 2.5 GSC5815-01190 light curve data, models, and residuals. Isothermal models are fitted separately to the bottom and top half of the light curve with results in Table 2.5. The half-light level was fixed based on the value expected for an event at the latitude of Saturn. The residuals in the lower panels are weighted.

Table 2.2 Values obtained through separate isothermal model fits to the bottom, top and full 1994 light curve.

Fitted Parameter	1994 GSC5815-01190 Bottom Half	1994 GSC5815-01190 Top Half	1994 GSC5815-01190 Full Curve
Background Level	-0.0501±0.0132	-0.0488±0.0400	-0.0339±0.0096
Full Level	0.9132±0.0403	0.9829±0.0065	0.9839±0.0061
r_h (km)	60790	60790	60790
λ_{gh}	1391.99±168	1828.51±189.	1701.82±118.00

Table 2.3 Quantities derived from the values obtained by isothermal model fits in Table 2.5

Derived Parameter	1994 GSC5815-01190 Bottom Half	1994 GSC5815-01190 Top Half	1994 GSC5815-01190 Full Curve
Half-Light Radius	60826.4±2.8	60826.4±3.0	60826.4±2.5
gravity	884.62	884.62	884.62
H (km)	43.72±5.28	33.27±3.06	34.04±2.47
T_{iso}	115.27±12.00	87.74±6.95	82.83±5.62
P_h (μbar)	0.91±0.08	0.46±0.08	0.57±0.07
n_h (cm^{-3})	$(6.67\pm0.09)\times10^{13}$	$(4.42\pm0.07)\times10^{13}$	$(5.07\pm0.06)\times10^{13}$

Chapter 3

Inversions

3.1 Introduction

In this chapter we describe our numerical inversion procedure for retrieving atmospheric pressure, temperature and number density profiles. The initial conditions for inversions are derived based on isothermal model fits and structure profiles are derived without any assumption of an atmospheric model, except hydrostatic equilibrium and local spherical symmetry. The inversion procedure described here was used by Olkin (1996) to derive Triton's atmospheric structure profiles based on Tr60 and Tr148 occultations. Here we present basic equations of this method. Complete details including tests to validate the inversion procedure can also be found in Chapter 6 of Olkin (1996). In this chapter we concentrate on the error analysis of the inversion. Olkin (1996) used a scaling procedure as described in French *et al.* (1978) to estimate the uncertainties in derived profiles. Here we numerically solve for these uncertainties.

3.2 Method

Inversions have been successfully used to derive structure parameters in various studies (Wasserman and Veverka 1973, see review by Hunten and Veverka 1976). Although equivalent in nature, these methods vary in the details. The method that we have used is similar to the method described by French *et al.* (1978), but our method does not rely on large-planet assumptions. In general our method was devised to be used with observations of planets of any size with no assumptions such as the scale height is much smaller than the radius of the occulting body.

The method described here was derived by Elliot (1989, unpublished notes) and was successfully utilized by Olkin (1996) to invert the light curves obtained during the Tr148 and Tr60 occultations. Due to the differences in the observational methods, a slightly different

method is used to invert the radio occultation data obtained with spacecraft and is described by Tyler *et al.* (1986).

The assumptions we have made in the derivation of profiles are:

(a) The main source of stellar light attenuation is differential refraction, where the refraction angle is small. We have neglected extinction due to scattering and absorption. As we discussed in Section 2.4, however, we find some evidence for effect on clouds on Earth's atmosphere in some of our data.

(b) There is no ray crossing, that is ray arriving at Earth is in the same radial order as they encountered Saturn's atmosphere. As we study on Section 3.3 based on simulated light curves, this assumption may not be valid in the deepest probed layers and slow events such as the 1995 GSC5249-01240 occultation.

(c) The atmospheric refractivity varies only with radius. This is same as assuming a spherically symmetric atmosphere with no horizontal gradients in the refractive index.

(d) The star is considered as a point source. But as we find later, the star is not a point source but has a certain size which can be calculated through an analysis of the power spectrum fluctuations of the occultation light curve about a local mean. This value is known as the star diameter (that is the diameter of the angular size of the star projected on the plane perpendicular to the view axis, at Saturn's distance), which generally lies in the range 3 to 10 km, i.e. small compared to the scale height of about 50 km. Thus, any thermal structures with spatial scales smaller than the stellar size are smoothed out. However, when the star dives in the atmosphere, its image is flattened proportionally to the normalized stellar flux: The vertical structures of the atmosphere are less and less smoothed. Thus, structures smaller than the star diameter can be detected in the lower part of the profile (Young 1976).

(e) The atmosphere is assumed to be a perfect mixture of hydrogen and helium in hydrostatic equilibrium. Any uncertainties in the composition is not considered in our inversion methods.

The normalized flux $\varphi(r)$ received by an observer at the shadow plane is related to the body plane radius r and shadow plane radius ρ through (ignoring extinction effects)

$$\varphi(r) = \frac{r}{\rho(r)}\left|\frac{dr}{d\rho(r)}\right|.$$ (3.1)

In the inversion procedure, we obtain an array of normalized flux (ϕ_k). From astrometry, we also have a corresponding array of shadow plane distances (ρ_k). Thus, we can reproduce equation 3.1 as:

$$\phi_k \rho_k \Delta\rho_k = r_k \Delta r_k,$$ (3.2)

where r_k is the corresponding planet plane radius.

$\phi(*) \Delta r(k) = \phi(k) \Delta\rho(k)$ (Geometric optics law.) $\Delta\theta(k) = \theta(k+1/2) - \theta(k-1/2)$
$\Delta\rho(k) = \rho(k+1/2) - \rho(k-1/2)$ $\rho(k) = r(k) + D\,\theta(k)$
$\Delta r(k) = r(k+1/2) - r(k-1/2)$ $\Delta\rho(k) = \Delta r(k) + D\,\Delta\theta(k)$
$r(k) = [r(k+1/2) + r(k-1/2)] / 2$ θ and $\Delta\theta$ are both negative quantities.
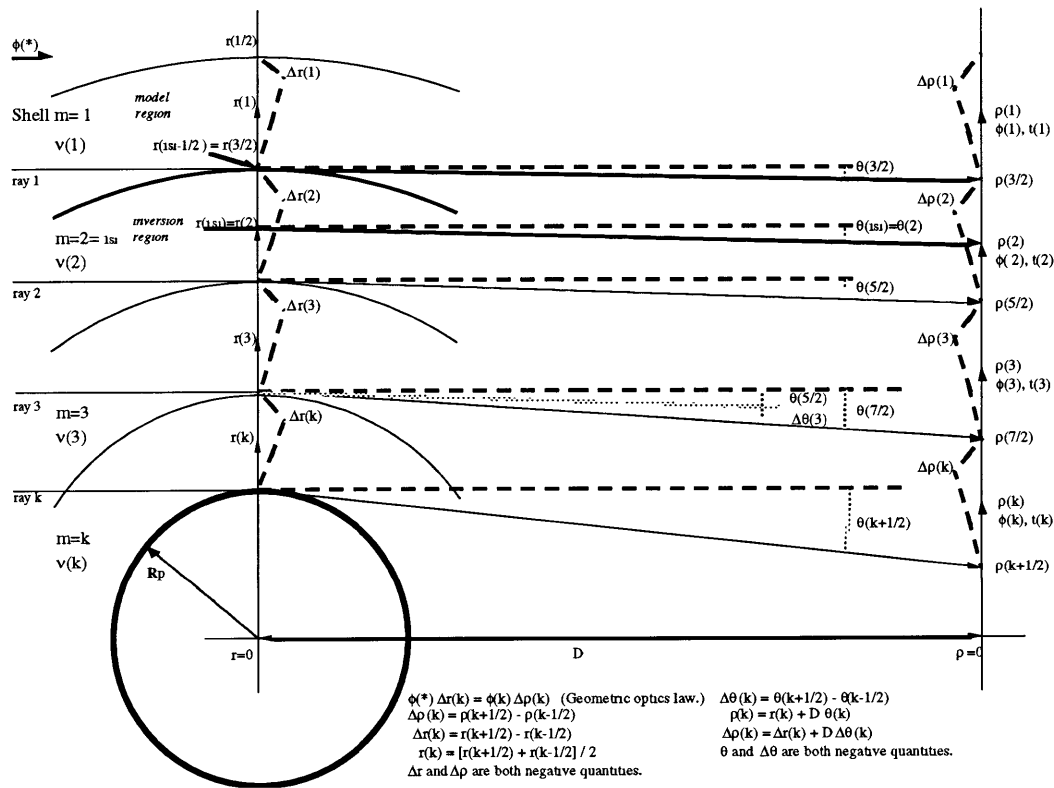Δr and $\Delta\rho$ are both negative quantities.

Figure 3.1   Stellar occultation by a planetary atmosphere. The figure above is reproduction of Figure 2.1 but refraction bending is represented as shells to describe the numerical inversion procedure. The figure is reproduced from Olkin (1996).

41

As shown in Figure 3.1 we can use half-indices to write the radii as (assuming r_k varies linearly)

$$2\phi_k \rho_k \Delta \rho_k = r^2_{k+1/2} - r^2_{k-1/2}.$$ (3.3)

Since we are dealing with an iteration we can write equation 3.3 with an initial r and a summation. The initial r will be based on the modeling procedure to the point where inversion begins. The radius to the kth shell will be:

$$r_{k+1/2} = \sqrt{r^2_i + 2\sum_{j=i}^{k} \phi_j \rho_j \Delta \rho_j},$$ (3.4)

where r_i is the initial radius. The error associated with $r_{k+1/2}$ then is:

$$\sigma^2(r_{k+1/2}) = \left(\frac{\partial r_{k+1/2}}{\partial r_i}\right)^2 \sigma^2(r_i) + \sum_{j=i}^{k}\left[\left(\frac{\partial r_{k+1/2}}{\partial \phi_j}\right)^2 \sigma^2(\phi_j) + \left(\frac{\partial r_{k+1/2}}{\partial \rho_j}\right)^2 \sigma^2(\rho_j)\right].$$ (3.5)

Here, we make a simplification by assuming that $\sigma(\rho_j)$ is small compared to the rest. Substituting $r_{k+1/2}$ and simplifying we get:

$$\sigma^2(r_{k+1/2}) = \frac{r^2_i \sigma^2(r_i) + \left(\sum_{j=i}^{k} \rho_j \Delta \rho_j \sigma(\phi_j)\right)^2}{r^2_i + 2\sum_{j=i}^{k} \phi_j \rho_j \Delta \rho_j}.$$ (3.6)

The angle θ was derived earlier in Chapter 2 based on optical geometry of a propagating ray refracting at very small angles. As for $r_{k+1/2}$, we can introduce the corresponding bending angle in half-indices as:

$$\theta_{k+1/2} = \frac{\rho_{k+1/2} - r_{k+1/2}}{D},$$ (3.7)

where D is the distance to the planet. The error associated with $\theta_{k+1/2}$ is then:

42

$$\sigma^2(\theta_{k+1/2}) = \frac{\sigma^2(r_{k+1/2})}{D^2},$$
(3.8)

where we have again assumed that astrometric error $(\rho_{k+1/2})$ is negligible.

The refractivity is derived based on changes of θ rather than $\theta_{k+1/2}$. The change in bending angle across the shell is:

$$\Delta\theta_k = \theta_{k+1/2} - \theta_{k-1/2}.$$
(3.9)

The error in $\Delta\theta_k$ is:

$$\sigma^2(\Delta\theta_k) = \sigma^2(\theta_{k+1/2}) + \sigma^2(\theta_{k-1/2}).$$
(3.10)

Because of noise and spikes, the flux is occasionally negative. To avoid problems with negative flux, the data are binned until the change in radius equal the shell size. The change in radius from one end of a shell to the other is written as:

$$\Delta r_k = r_{k+1/2} - r_{k-1/2}.$$
(3.11)

We define a mid-shell radius as:

$$r_k = \frac{1}{2}\left(r_{k+1/2} - r_{k-1/2}\right).$$
(3.12)

The error in the mid-shell radius is:

$$\sigma(r_k) = \frac{1}{2}\sqrt{\sigma(r_{k+1/2})^2 + \sigma(r_{k-1/2})^2}.$$
(3.13)

Refractivity is computed by inverting the equation for the bend angle of a ray through a spherically symmetric atmosphere (Elliot 1989, unpublished notes). This is given by:

$$\nu(r) = \exp\left[\frac{1}{\pi}\int_{r'=r}^{r'=\infty} \cosh^{-1}\left(\frac{r'}{r}\right)d\theta(r')\right] - 1,$$
(3.14)

43

where r' is an integration variable. Since refractivity is small ($\sim 10^{-10}$) the exponential can be expanded to the first order and the result can be written as:

$$V_{k+1/2} = -\frac{1}{\pi}\left[\int\limits_{r'=r_i}^{r'=\infty} \cosh^{-1}\left(\frac{r'}{r_{k+1/2}}\right)d\theta(r') + \sum_{j=i}^{k}\cosh^{-1}\left(\frac{r_j}{r_{k+1/2}}\right)\Delta\theta(r_j)\right].$$ (3.15)

The error in refractivity is calculated through:

$$\sigma^2(V_{k+1/2}) = \sigma^2\left(\frac{1}{\pi}\int\limits_{r'=r_i}^{r'=\infty}\cosh^{-1}\left(\frac{r'}{r_{k+1/2}}\right)d\theta(r')\right) + \sigma^2\left(\frac{1}{\pi}\sum_{j=i}^{k}\cosh^{-1}\left(\frac{r_j}{r_{k+1/2}}\right)\Delta\theta(r_j)\right).$$ (3.16)

We can separately evaluate the variances of the two terms. At the large planet limit the significant error arises from the determination of $\theta(r_j)$, $r_{k+1/2}$, and r_j. These three random variables are all perfectly correlated as they are proportional to each other. The 3 correlation coefficients $\rho_{r_{k+1/2}r_j}$, $\rho_{r_{k+1/2}\Delta\theta(r_j)}$ and $\rho_{r_j\Delta\theta(r_j)}$ are equal to one, where as the correlation coefficient $\rho_{r_ir_{k+1/2}}$ is equal to zero as the two are independent of each other. Using partials we can write the variances as:

$$\sigma^2(V_{k+1/2}) = \begin{bmatrix}\left(\dfrac{\partial}{\partial r_{k+1/2}}\dfrac{1}{\pi}\int\limits_{r'=r_i}^{r'=\infty}\cosh^{-1}\left(\dfrac{r'}{r_{k+1/2}}\right)d\theta(r')\right)^2\sigma^2(r_{k+1/2}) + \\[2em] \left(\dfrac{\partial}{\partial r_i}\dfrac{1}{\pi}\int\limits_{r'=r_i}^{r'=\infty}\cosh^{-1}\left(\dfrac{r'}{r_{k+1/2}}\right)d\theta(r')\right)^2\sigma^2(r_i) + \\[2em] \left(\dfrac{\partial}{\partial r_{k+1/2}}\dfrac{1}{\pi}\sum_{j=i}^{k}\cosh^{-1}\left(\dfrac{r_j}{r_{k+1/2}}\right)\Delta\theta(r_j)\right)^2\sigma^2(r_{k+1/2}) + \\[2em] \left(\dfrac{\partial}{\partial r_j}\dfrac{1}{\pi}\sum_{j=i}^{k}\cosh^{-1}\left(\dfrac{r_j}{r_{k+1/2}}\right)\Delta\theta(r_j)\right)^2\sigma^2(r_j) + \\[2em] \left(\dfrac{\partial}{\partial\Delta\theta(r_j)}\dfrac{1}{\pi}\sum_{j=i}^{k}\cosh^{-1}\left(\dfrac{r_j}{r_{k+1/2}}\right)\Delta\theta(r_j)\right)^2\sigma^2(\Delta\theta(r_j))\end{bmatrix}.$$ (3.17)

44

The number density at the $k+1/2$ shell is:

$$n_{k+1/2}(r) = \frac{L}{\pi \upsilon_{STP}} V_{k+1/2}(r).$$ (3.18)

The error in $n_{k+1/2}(r)$ is:

$$\sigma^2\left(n_{k+1/2}(r)\right) = \frac{L}{\pi \upsilon_{STP}} \sigma^2\left(V_{k+1/2}\right).$$ (3.19)

The equation for the pressure, $p(r)$, is found by integrating the equation of hydrostatic equilibrium:

$$dp(r) = -g\mu m_{amu} n(r) dr.$$ (3.20)

Using the half-indices notation we can write this as:

$$p(r_{k+1/2}) = -\frac{L\mu m_{amu} GM_p}{\pi V_{STP} r_{k+1/2}} \left[\begin{array}{l} \int_{r'=r_i}^{r'=\infty} \cosh^{-1}\left(\frac{r'}{r_{k+1/2}}\right) - \sqrt{1 - \left(\frac{r_{k+1/2}}{r'}\right)^2} \, d\theta(r') + \\ \sum_{j=i}^{k} \cosh^{-1}\left(\frac{r_j}{r_{k+1/2}}\right) - \sqrt{1 - \left(\frac{r_{k+1/2}}{r_j}\right)^2} \, \Delta\theta(r_j) \end{array} \right].$$ (3.21)

As in refractivity we can calculate the error associated with pressure:

$$\sigma^2\left(p_{k+1/2}\right) = -\frac{L\mu m_{amu} GM_p}{\pi V_{STP} r_{k+1/2}} \left[\begin{array}{l} \sigma\left(\int_{r'=r_i}^{r'=\infty} \cosh^{-1}\left(\frac{r'}{r_{k+1/2}}\right) - \sqrt{1 - \left(\frac{r_{k+1/2}}{r'}\right)^2} \, d\theta(r')\right)^2 + \\ \sigma\left(\sum_{j=i}^{k} \cosh^{-1}\left(\frac{r_j}{r_{k+1/2}}\right) - \sqrt{1 - \left(\frac{r_{k+1/2}}{r_j}\right)^2} \, \Delta\theta(r_j)\right)^2 \end{array} \right].$$ (3.22)

45

Using the derivatives we can write the variances in equation 3.22 as:

$$\sigma^2\left(p_{k+1/2}\right) = -\frac{L\mu m_{amu}GM_p}{\pi V_{STP}r_{k+1/2}}\left[\begin{array}{l}\left(\frac{\partial}{\partial r_{k+1/2}}\int_{r'=r_i}^{r'=\infty}\cosh^{-1}\left(\frac{r'}{r_{k+1/2}}\right)-\sqrt{1-\left(\frac{r_{k+1/2}}{r'}\right)^2}\,d\theta(r')\right)^2\sigma^2(r_{k+1/2})+\\[4mm]\left(\frac{\partial}{\partial r_i}\int_{r'=r_i}^{r'=\infty}\cosh^{-1}\left(\frac{r'}{r_{k+1/2}}\right)-\sqrt{1-\left(\frac{r_{k+1/2}}{r'}\right)^2}\,d\theta(r')\right)^2\sigma^2(r_i)+\\[4mm]\left(\frac{\partial}{\partial r_{k+1/2}}\sum_{j=i}^{k}\cosh^{-1}\left(\frac{r_j}{r_{k+1/2}}\right)-\sqrt{1-\left(\frac{r_{k+1/2}}{r_j}\right)^2}\,\Delta\theta(r_j)\right)^2\sigma^2(r_{k+1/2})+\\[4mm]\left(\frac{\partial}{\partial r_j}\sum_{j=i}^{k}\cosh^{-1}\left(\frac{r_j}{r_{k+1/2}}\right)-\sqrt{1-\left(\frac{r_{k+1/2}}{r_j}\right)^2}\,\Delta\theta(r_j)\right)^2\sigma^2(r_j)+\\[4mm]\left(\frac{\partial}{\partial\Delta\theta(r_j)}\sum_{j=i}^{k}\cosh^{-1}\left(\frac{r_j}{r_{k+1/2}}\right)-\sqrt{1-\left(\frac{r_{k+1/2}}{r_j}\right)^2}\,\Delta\theta(r_j)\right)^2\sigma^2(\Delta\theta(r_j))+\end{array}\right]$$

$$(3.23)$$

The temperature is derived from the pressure and number density using the ideal gas law. We note here that since the scale height is derived as a ratio of the two differently weighted integrals of the same variable in equations 3.15 and 3.22, which it is independent of the atmospheric composition, much of the noise cancels out, and as a consequence of this the scale height profiles have smaller fractional errors than number density and pressure profiles.

3.3 Tests of the Method

Olkin (1996) Section 6.2 contains a description of the tests that were performed to check the validity of inversion procedure. Although much better than an isothermal fit to the observed light curve, the inversion method has several limitations. Among these limitations are that the retrieved profiles are exponentially sensitive to a given error as higher levels are probed, and that different initial conditions in the inversion procedure can produce different profiles. In order to address the issues associated with errors and initial conditions, here

46

in this section we concentrate on testing the error analysis of our method. The sensitivity of profiles to errors were earlier studied by Wasserman and Veverka (1973) and French *et al.* (1978). These authors showed in particular that during the inversion once 3 scale heights has been probed after the initial point of integration, the relative error made on the temperature profiles is less than 2%. But the determination of background level affects greatly as the inversion is equivalent to an integration of the stellar flux.

The nature of the inversion equations are directly related to the fact that different profiles could be produced with different initial conditions. This point is illustrated in Figure 3.2 and 3.3, where we initiated the inversion at different flux levels. The error induced by the uncertainty in different initial conditions damps exponentially as deeper zones are probed, in agreement with our error equations as well as prior predictions. In all cases, the extreme profiles do not differ by more than 1 K at the lowest radius probed.

To illustrate features associated with the inversion, we have utilized the equations developed in Section 3.2 to invert an isothermal light curve with added random noise. For this case we let scale height, H = 10 km, perpendicular velocity, $v_\perp = 10$ km s^{-1}, and standard deviation of noise, $\varepsilon(\phi) = 0.02$. These parameters give a noise factor of

$$\left(\frac{v_\perp}{H}\right)^{\frac{1}{2}} \varepsilon(\phi) = 0.02,$$ comparable to the isothermal light curve used by

French *et al.* (1978) to investigate their inversion procedure. The light curve they used was created through results from the Kuiper observations of the occultation of ε Gem by Mars. Here, our light curve was created based on the IRTF observations of the occultation of Tr148 by Triton using the methods derived in Chapter 2. The light curve is shown in Figure 3.4. The solid line is the noise-free isothermal light curve.
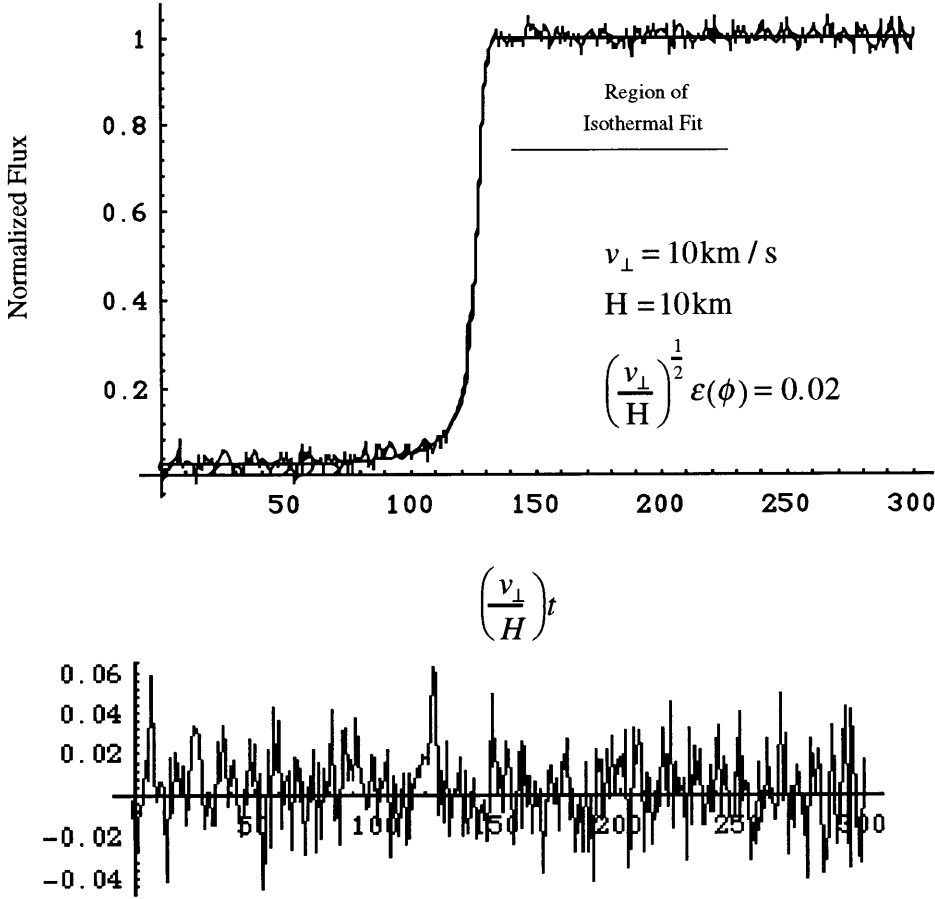
Figure 3.2 Synthetic isothermal light curve with scale height H=10 km

and noise figure $\left(\dfrac{v_\perp}{H}\right)^{\frac{1}{2}}\varepsilon(\phi)=0.02$. The solid line is the noise-free light

curve. The bottom profile is the added noise. The results of the inversion of noisy light curve is shown in Figures 3.5 and 3.6.

Two methods were used to deduce the scale height. The first utilizes the isothermal fit to the data. The second was the inversion procedure from a flux level of 0.78. The initial conditions for inversion was derived based on isothermal fit till a flux level of 0.78 as illustrated in Figure 3.4. The isothermal model fit to the complete light curve produced a scale height of 9.77 ± 0.87 km. The results for the inversion is shown in Figure 3.5. The error bars on the scale height profile were computed using the methods described in section 3.2, and have a total length of one standard deviation. At all altitudes, the error bars are consistent with the actual scale height of 10 km.
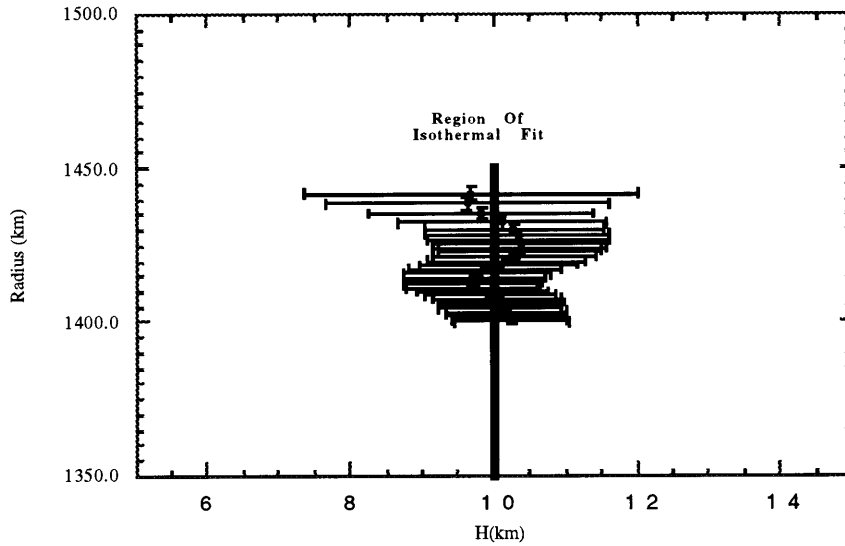
Figure 3.3 Scale Height profile obtained from inversion of the light curve shown in Figure 3.1. The true scale height is 10 km. We have shown both errors in scale height and radius at one standard deviation.

We have also shown the errors in altitude, which is at a level of 1 km at the top of the profile to a level of 0.5 km at bottom. The characteristic of the cosh term in the refractivity and pressure integrals is reflected in the errors of the scale height profile: the errors are initially very large, and eventually minimize at about three scale heights from the beginning of inversion and after they remain constant. The minimum scale height obtained with the inversion is 10.24±0.79. Based on these two values the fractional error, $\left.\dfrac{\sigma(H)}{H}\right|_{min}$, of the inversion method is 0.079 where as for the isothermal method is 0.089. The minimum value predicted by French *et al.* 1978 (with the large planet approximations is) 0.039. We find that our error for the inversion is a factor 2 greater than expected from the method of French *et al.* 1978. Though the error bar predicted by them (Equation B-13 and B-14) is smaller for this small planet synthetic light curve inversion, when we apply the inversion and error analysis to Saturn, a large planet, we find errors which agree with the predictions. Therefore we conclude here that the significant difference between their work and our work is that the intensity spikes observed in our light curves have non-Gaussian

49

statistical distributions. French et al. (1978) assumes that noise distribution is Gaussian in deriving their equations B-13 and B-14.

Table 3.1 Comparison between our results and predictions of French *et al.* 1978

Parameter	1989 28 Sgr	1994 GSC5815-01190	1995 GSC5249-01240
$\varepsilon(\phi)$	0.035	0.065	0.090
Model Fits, H (km)	56.01 ± 1.73	34.04 ± 2.47	44.32 ± 3.55
$\dfrac{\sigma(H)}{H}\Big|_{ModelFits}$	0.033	0.072	0.080
$\dfrac{\sigma(H)}{H}\Big|_{predicted}$ 1	0.034	0.075	0.017
Inversions, H (km)	59.74 ± 1.61	34.67 ± 2.41	35.22 ± 1.50
$\dfrac{\sigma(H)}{H}\Big|_{inversions}$	0.026	0.069	0.042
$\dfrac{\sigma(H)}{H}\Big|_{predicted}$ 2	0.043	0.094	0.025

Table Notes:
1. French *et al.* 1978 equation B-13 (for isothermal model fits).
2. French *et al.* 1978 equation B-14 (for inversions).

As tabulated in Table 3.1 we find that in general inversions have fractional errors less than those obtained by isothermal fits. For the 28 Sgr and GSC5815-01190 inversions we find that the predicted error is greater than by at least 35% from the value we have obtained by our method, where as the values obtained by isothermal fits agree within 4%. The GSC5249-01240 curve disagrees with both predictions for isothermal fits and inversions by providing values which are greater than predicted. We believe this is due to the large number of spikes in the light curve and separately in Section 2.4 we have addressed this issue.
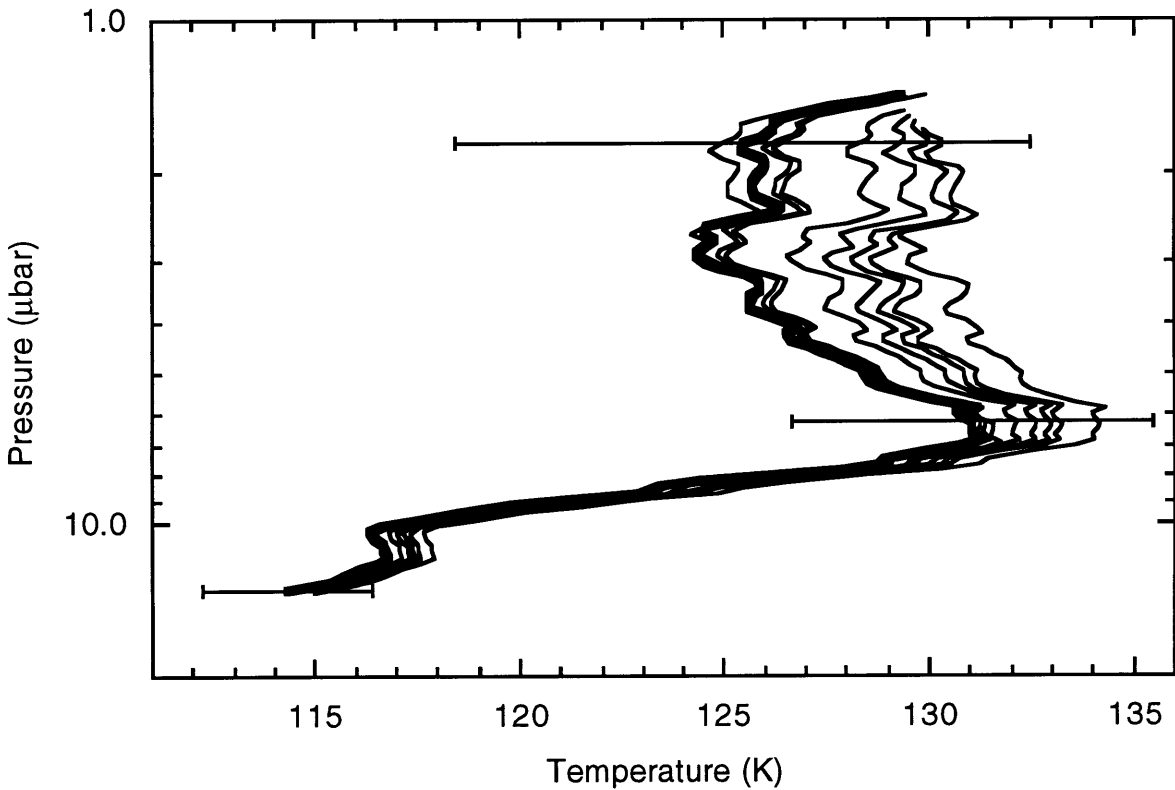
50

3.4 Application to Saturn events

Figure 3.4. The inversion algorithm applied to the November 20, 1995 GSC5249-01240 immersion data. The different temperature profiles correspond to the different initial conditions by varying the starting point of numerical inversion based on different model fits. Even though these is a slight divergence at the top level of the inversion, the values converge at the bottom to a steady temperature of 115 K. The thicker line in the middle is the preferred temperature profile. The horizontal lines shown here are the inversion temperature errors shown here are primarily due to the error in initial conditions and flux errors, as formulated by French *et al.* (1978).

We used the three light curves to invert using the method described in Section 3.2. Prior to inversion the light curves were normalized with the background and top level defined by isothermal fits. As illustrated by Olkin (1996) a 5% error in the determination of the background level causes the temperature at the lowest level probed to deviate by about 2 K, which is within the 1σ error at the lowest level probed. It is highly unlikely that our background calibration is off more than 5%. Synthetic light curves created by changing the background level agreed with the results obtained by Olkin (1996).
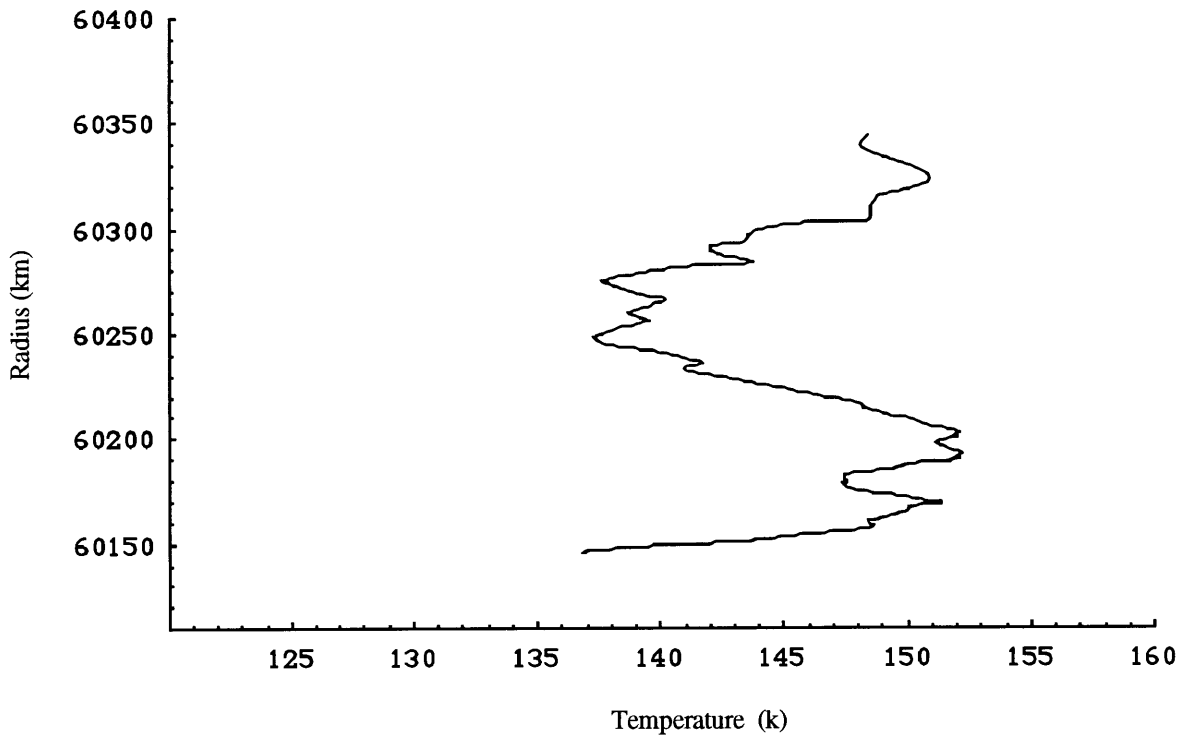

Figure 3.5 The inversion algorithm applied to the July 3, 1989 28 Sgr immersion data. This temperature profile depicts several important features at the altitude range probed by the occultation. Among this is a warm layer at a radius of 60150 km, where the temperature increases by 14K in 15 km, and decreases again by the same amount in 80 km altitude. A characteristic of thus feature is its asymmetry, the lower gradient being larger than the upper one. The increase in temperature continues again from a radius of 60260 km at a lower positive gradient the one below at a radius of 60150 km. This behavior in the temperature profile agrees with a vertical propagating wave of wavelength of about 200 km, corresponding to inertial-gravity waves.

The temperature profiles from the numerical inversion of GSC5249-01240 light curve is shown in Figure 3.4, which we have described in terms of different initial conditions. As shown in this plot, all profiles agree at the lowest level less than 2 K, which is expected based on the mathematical nature of the inversion equations. We have also shown the H97 model and the temperature defined by isothermal fits. The GSC5249-01240 temperature profile is colder from H97 model at an average of 20 K, where as the H97 model agrees with the 28 Sgr profile (Figure 3.5). Also both 28 Sgr and GSC5249-01240 profiles are inconsistent with an isothermal model.

In 1989 and 1995 the two events were observed at two different latitudes on Saturn. And the profiles show that Saturn's atmosphere is highly variable. We can describe non-isothermal structures which appear on the temperature profiles.

Though our sample is only two light curves, and thus very small, the structures found here need to be investigated with more profiles as occultations are observed. A main feature on the GSC5249-01240 profile is a warm layer, above 10 μbar level where temperature increases by 15 K in 20 km, and begins to decrease slightly at a very low rate. We find a temperature gradient of 0.41 ± 0.09 K km^{-1} for the radius region probed, between 54840 and 54860 km, a radius scale less than the scale height. We investigate below qualitatively the possibility that this feature is caused by waves propagating on the stratosphere. The slight variations in the temperature structure that correlate with the spikes in the light curve is considered as well-mixed layers of buoyancy-driven turbulence. The length scale for these variations are less than 2 km, where as temperature variations range from 1.5 to 4.5 K.

The high gradient feature found on the GSC5249-01240 light curve has also been observed in temperature profiles for Uranus and Neptune obtained with visible and infrared occultations (Roques *et al.* 1995, Baron *et al.* 1989). The 22 light curves analyzed by Roques *et al.* (1994) showed that these features would disappear, possibly through thermal conduction, in a few hours for the smaller observed structures (a few degrees Kelvin in amplitude extending over few kilometers in height) to a few months for the larger ones (20K or so in amplitude extending over one scale height). Consequently, the thermal contrast must be renewed by some process, which is still unknown for the present time. For Neptune the possibility of very localized heating by aerosol or hydrocarbon layers has been discarded

53

by Roques *et al.* (1994) as the heating mechanisms need some very efficient confinement methods.
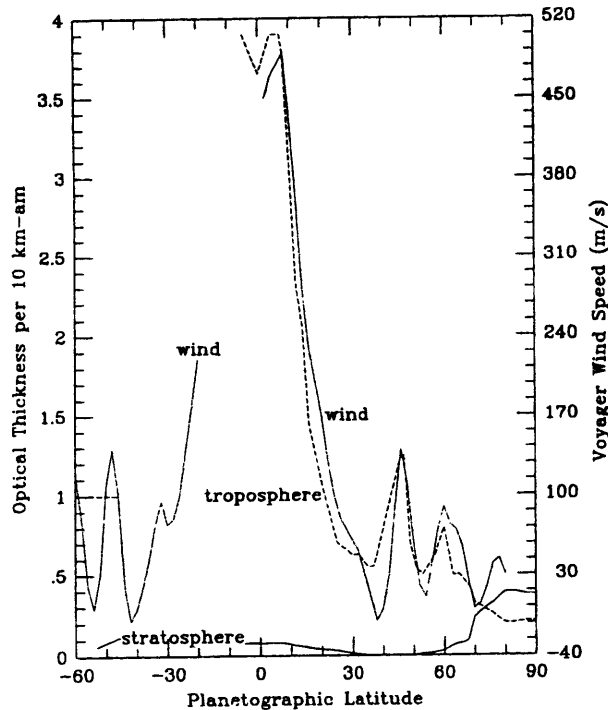

Figure 3.7 Latitudinal variation of Stratospheric and tropospheric optical thickness per 10km-am layer, compared with Voyager wind speeds (Smith et al. 1982). The strongest increase of stratospheric optical depth occurs at around 70 degrees north (the dark line labeled stratosphere). The haze extends into the higher stratosphere above the mbar level, thus allowing the idea that stratospheric aerosols in the high latitudes are quite different from the tropospheric particles. Tropospheric optical depth is shown by dashed lines, which follow a similar distribution as the zonal wind velocities (labeled winds). Figure is reproduced from Karkoschka and Tomasko (1993).

Dynamical mechanisms, such as propagating waves, were suggested for explaining the rapidly changing aspect of the thermal profiles both in time and amplitude. The question that needs to be answered for Saturn is can these waves, if exist, provide the necessary heating mechanism through viscous damping of waves.

Another mechanism for heating the stratosphere is aerosols. Even though there may be dynamical difficulties to maintain such layers in the equatorial regions of Saturn, Karkoschka and Tomasko (1993) have observed the higher latitudes of Saturn in search of hazes with HST. Optical depths in ultraviolet of hazes at latitudes above 70 degrees north were found to be almost unity, where as no existence of hazes were found in low and mid-southern latitudes. The tropospheric haze distribution is completely different from the

54

distribution of stratospheric haze, since optical depths in the stratosphere strongly increase from the north pole to equator.

In Figure 3.7 we have reproduced the latitudinal variation of stratospheric and tropospheric optical thickness, which has been compared with Voyager wind speeds by Karkoschka and Tomasko (1993). Three facts have shown that the stratospheric aerosols in the high latitudes are quite different from the tropospheric particles, and that they are produced by different mechanisms. First the difference in optical constants for the two different aerosols is so much larger that it is difficult to construct a model where the two type particles have the same values. Second, the stratospheric aerosols at these latitudes have to be present in high concentrations almost to the top of the atmosphere to agree with observations, while the tropospheric particles, uniformly mixed with gas below about 100 mbar, are found in comparable concentrations only quite low in the atmosphere. Third, there is an indication that the haze optical depth in the stratosphere is somewhat concentrated to the top half rather than uniformly mixed. In the polar region it seems clear that the stratospheric and tropospheric particles are produced in completely different ways and have different compositions.

Given the lack of aerosols at mid-latitudes, it seems possible that the mechanism of formation of stratospheric particles is different at polar and equatorial latitudes. In the polar region, a mechanism in which the particles are produced at very high latitudes are required. A similar problem exist in the case of Uranus. For the latter planet, the possibility has raised that dust material could be provided by the Uranian ring particles spiraling inward and eventually settling down in the stratosphere (Sicardy *et al.* 1985). This problem is addressed in details by Rizk and Hunten (1990), who conclude that a typical dust mass influx of 10^{11} g year^{-1} from the Uranian rings can provide a temperature rise of up to 50 K in the 1-10 μbar region. The corresponding heating rate is in the range $10^{-6} - 10^{-10}$ erg cm^{3}s^1 for particles of size 1 μm. Such aerosols have been found to be a good candidate for heating the occultation region, in view of the other heating rates at these atmospheric level.
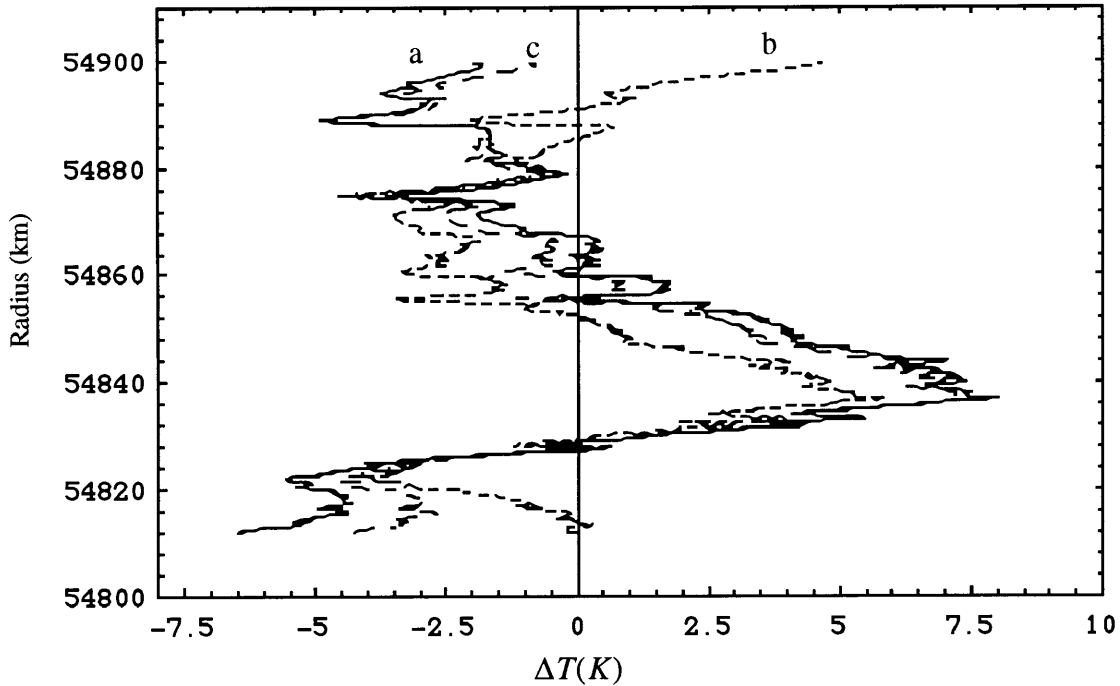
Figure 3.8 Sensitivity of the 1995 temperature profile to the mean temperatures. Here we have shown the temperature profile minus a mean profile, as a function of the radius. The 3 different ΔT profiles were determined based on three different possible definitions of mean temperature: (a) linear, assuming the mean profile between 54800 and 54900 km is made of constant temperature gradient, term as well, and (b) constant flux, assuming $T^b \dfrac{dT}{dz}$ is a constant, where b=0.75, so that $T^{1.75}$ is linear,(c) quadratic, assuming the mean profile has a quadratic temperature.

If such an argument is applied to Saturn, we would expect a homogeneous distribution of haze particles at stratosphere rather than high concentrations at polar regions, as suggested for Uranus. Because of this reason, whether the same mechanism may be applied to Saturn is unclear. A magnetic connection for Saturn's rings and atmosphere has been suggested by Connerney (1986). The latitudinal variations in images of Saturn's disk, upper atmospheric temperatures from Voyager observations, and ionospheric electron densities are found in magnetic conjugacy with features in Saturn's ring plane. These variations were described as the result of a variable influx of water, transported along magnetic field lines from sources in the ring plane.
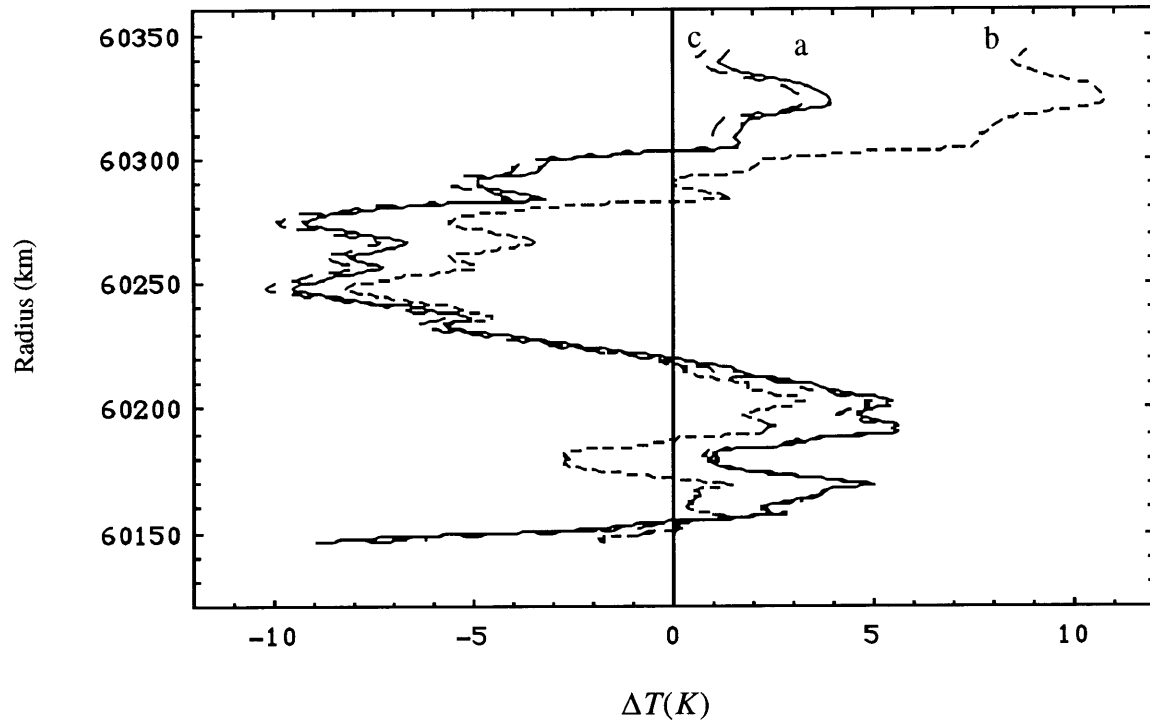
56

Figure 3.9 Sensitivity of the 1989 temperature profile to the mean temperatures. Same as Figure 3.10.

The static stability, s, of a vertical atmosphere can be defined as:

$$s = \frac{dT}{dz} + \Gamma \tag{3.24}$$

where $\frac{dT}{dz}$ is the observed vertical temperature gradients and Γ is the adiabatic lapse rate defined as:

$$\Gamma = \frac{g}{c_P} = -\frac{dT}{dz}\bigg|_{\text{adibatic}} . \tag{3.25}$$

In general an atmosphere is considered to be stable if $s > 0$ $\left(\frac{dT}{dz} > \frac{dT}{dz}\bigg|_{\text{adibatic}}\right)$. As shown in Figure 3.10, the GSC5249-01240 occultation indicates lapse rates very close and sometimes less than the local adiabatic rate occurring below 3 to 4 km level.
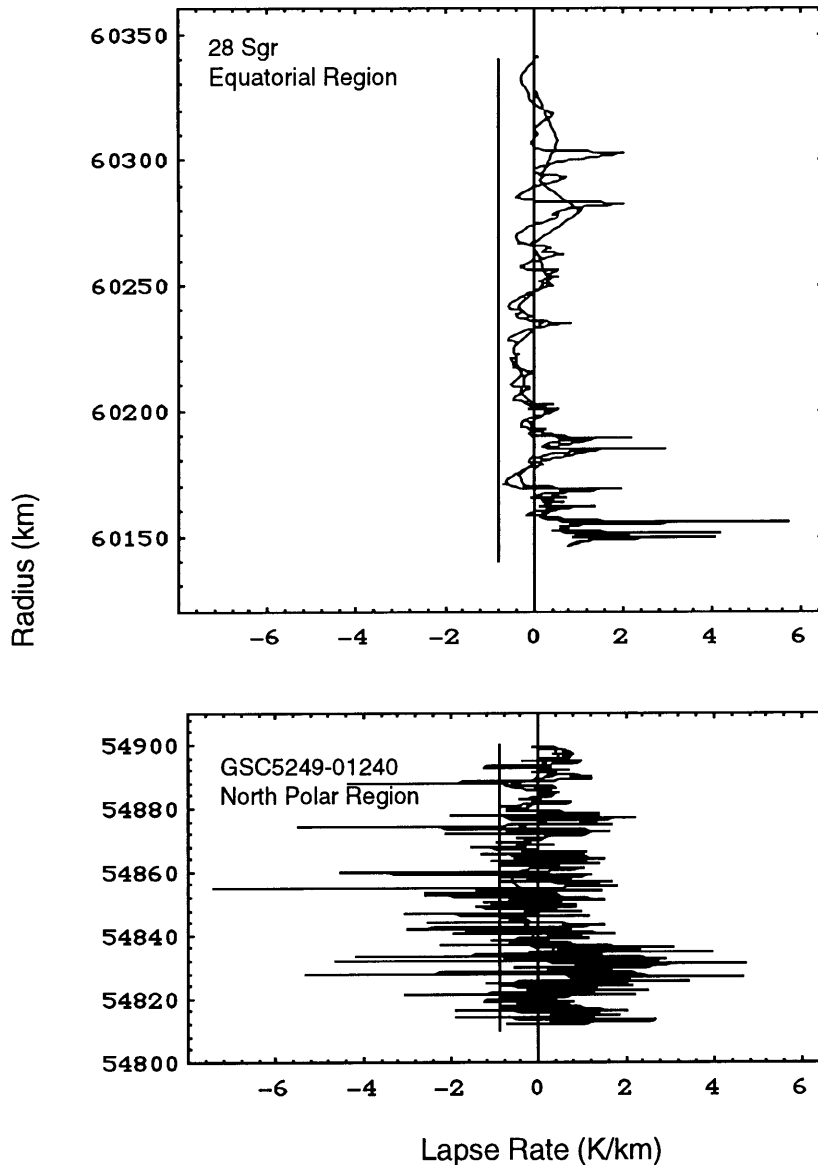
57

Figure 3.10 Here we have plotted the derivative of the temperature in the altitude range probed. (a) 28 Sgr The values range from –0.5 to 2 K km^{-1}, suggesting a downward energy flow from the thermosphere. Also the temperature derivatives are never near the adiabatic lapse rate, but is centered around zero suggesting a nearly isothermal atmosphere. (b) GSC5249-01240 Though at small times scales, with altitude ranges less than 3 km, the lapse rate is above the adiabatic lapse rate, in average the atmosphere is below or close to the level, suggesting that there are saturated gravity waves in this region. Turbulence activity may be expected at regions where lapse rate is higher than the adiabatic value and coincide with the observed spikes in the light curve. This is completely different from the high latitudes as shown in top curve.

The temperature gradients derived from the 28 Sgr immersion temperature profile from immersion observations at IRTF never reach the adiabatic value (lower curve), and suggest an isothermal basic state with a mean lapse rate of 0. On short scales the 28 Sgr temperature gradients imply convective turbulence, but not at a level implied by the GSC5249-01240 temperature gradients. Thus the level of turbulence activity observed in the equatorial region is completely different from that of the north polar region. We believe this is rather due to the fact that at the north polar region we have observed a primarily horizontal event rather than a vertical as in the equatorial region. But some of the structure observed in the temperature gradients are due to vertical changes, especially the 14 K temperature increase. We discuss below the reasons for observed high temperature gradients in the two curves.

Since the observed temperature gradients, if interpreted as vertical gradients, should suggest a super-adiabatic state, it is highly likely most of these temperature gradients are horizontal and not vertical. If these are in fact vertical gradients, then the north polar atmosphere is in an state not seen elsewhere. Such superadiabatic gradients have not been observed in any of the temperature profiles derived for giant planets based on stellar occultations so far. Another reason for not observing such low variations may be that none of the prior occultations achieved the high resolution we have observed due to the low velocity of the occultation. But none of these occultations probed a long horizontal structure as we did. Therefore we can set a lower limit on the horizontal variations by assuming the constraint that vertical temperature gradients should not exceed the adiabatic value. Currently no theory exists that would allow us to clearly state how much of the variations are horizontal rather than vertical.

In Figure 3.11 we show the horizontal temperature gradients by assuming all the temperature variations are due to horizontal structure. As shown in Figure 8 the horizontal temperature variations are less than a 1 K km^{-1}, and may be produced primarily due to gravitational waves. As suggested and discussed in Yelle *et al.* (1996), the convective turbulence behavior seen in the lapse rates from the temperature profiles occur when the amplitudes of gravity waves generated in the lower atmosphere becomes so large that the temperature gradient of the wave approaches the adiabatic value. At this point convective instability generates turbulence. Thus, the regions where the lapse rates are close to the adiabatic value are

probably associated with a well-mixed layers of buoyancy-driven turbulent regions. Physically, this may also correspond to the breaking of waves in these mixed layers, where breaking limits the further growth of the wave amplitude.
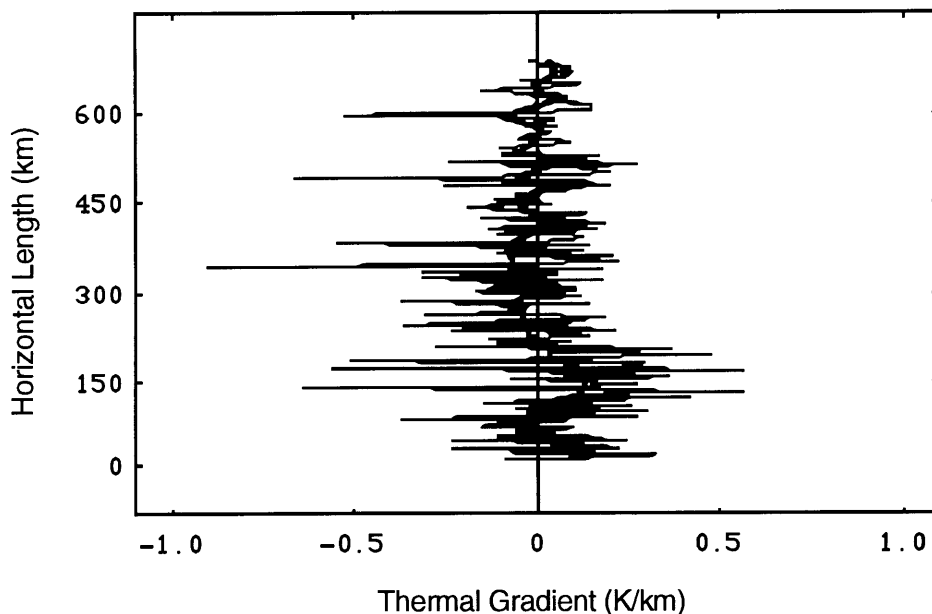

Figure 3.11 Temperature gradients of the GSC5249-01240 assuming that all variations are due to horizontal structure. As shown the horizontal gradients never exceed ± 1 K km^{-1}. Some of the gradients may be due to vertical variations rather than horizontal as implied here, but the purpose of this figure is to show that temperature variations may occur at the above level in horizontal directions.

3.5 Heating by Gravity Waves

The precise nature of the waves in Saturn's upper atmosphere can be deduced based on the observed temperature profiles. For giant planets two different modes, with two different frequencies, can explain the data. To distinguish between the two modes it is necessary one study the temperature structure resulting by considering each mode separately. If the main restoring force is buoyancy, then the transverse waves are important resulting in waves known as inertia-gravity waves at wavelengths less than or

60

equal to scale height and Rossby waves at wavelengths couple of scale heights long. If the restoring force is pressure, then the wave is longitudinal resulting in acoustic waves. The large wavelength Rossby waves are known to be involved in the stability of polar hexagon in Saturn and Red Spot in Jupiter, where temperature measurements with Galileo probe strongly suggests the existence of saturated gravity waves in Jupiter (Young *et al.* 1996). The limiting frequency which separates acoustic waves from inertia waves is called the Brunt-Vaisla frequency, η, given in equation 3.26.

Gravity waves are able to propagate vertically only if their Doppler shifted frequencies as measured in the local rest frame of the gas is less than the local Brunt-Vaisla frequency associated with the static stability. Otherwise they are evanescent waves, with amplitudes decaying exponentially with altitude. Evanescent waves have been considered by Friedson (1994) to explain the scintillations observed by Voyager on Titan's atmosphere. Mechanisms other than evanescence, such as wave transience, wave breaking, or propagation through a background meridional wind that varies with altitude may also lead to slow wave amplitude growth or amplitude decay with height.

The background atmospheric thermal structure will assert a significant influence over gravity wave propagation, since the amplitude and vertical wavelength of a vertically propagating wave will continually adjust in response to vertical variations of the stability. In the absence of damping, variations in the temperature profile should grow exponentially with height, for gravity waves, but in real atmospheres such growth is reduced by internal instabilities and by trapping and reflection of waves. French and Lovelace (1983) have modeled a situation where the eddy diffusivity is just sufficient to suppress the exponential growth, so that the fractional amplitude of the wave is constant with height.

The Brunt-Vaisla frequency, η, is equal to the observed temperature gradient and local adiabatic lapse rate through

$$\eta = \left[\frac{g}{T}\left(\frac{dT}{dz} + \frac{g}{C_p} \right) \right]^{\frac{1}{2}}$$

(3.26)

61

where C_p is the specific heat at constant pressure of 96% H and 4% He atmosphere. The Brunt Vaisla frequencies for the 28 Sgr observations are shown in Figure 3.11 and is calculated based on the temperature profile shown in Figure 3.6 and temperature gradient in Figure 3.12. For the 28 Sgr observations, the mean Brunt-Vaisala frequency corresponds to a period of about 2 min. This is in principle detectable if two nearby sites are used to probe the same region of Saturn's atmosphere, over an interval time of several minutes. This is in practice rather difficult because nearby sites usually probe nearby regions at interval of time of a few seconds only. Nevertheless, future occultation planning should consider some favorable geometry of observations, for which such an experiment could be achieved.

If we assume that the observed structures are gravity waves, not acoustic, these waves have been generated at the top of the convection zone, tropopause, through turbulent motions. According to Goldreich and Kumar (1990), the efficiency for the conversion of convective energy flux into the energy flux in gravity waves scales as the turbulent Mach number, which is the ratio of velocity fluctuations of the energy bearing eddies at the tropopause to the sound speed. For planetary atmospheres this ratio is less than one.
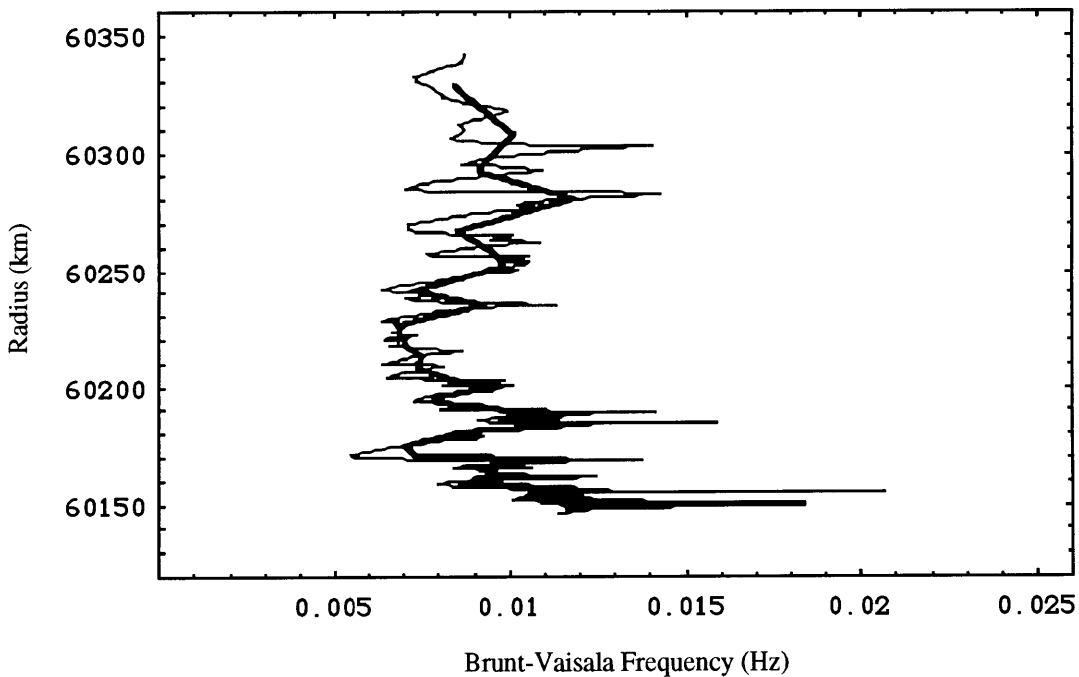

Figure 3.11 Brunt-Vaisla frequencies near the equator of Saturn based on temperature derivatives of 28 Sgr occultation.
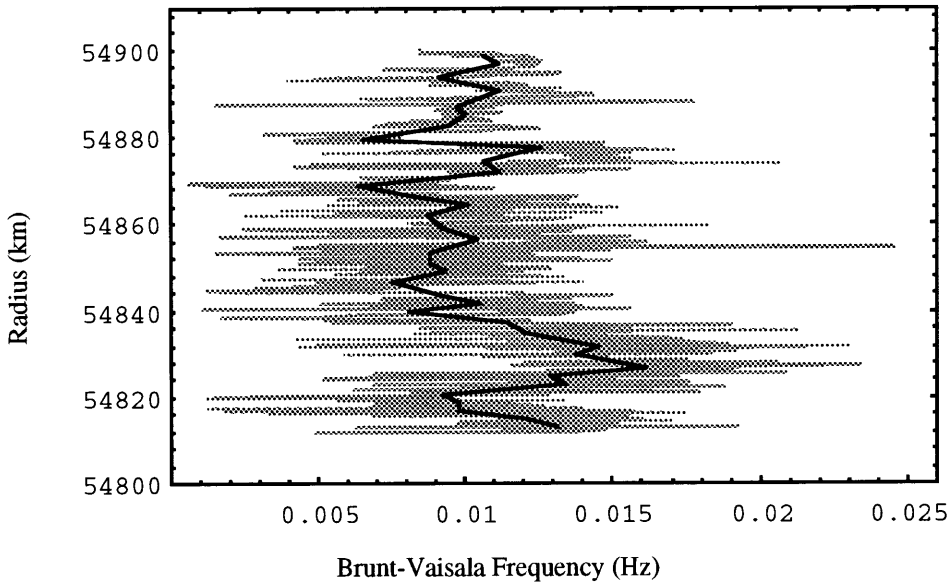
Figure 3.12   Brunt-Vaisla frequencies near the polar region of Saturn based on temperature derivatives of GSC5249-01240 occultation.

As studied by Dunham *et al.* (1980), a wave trapping mechanism can be considered based on a solution, χ to static stability equations, which can be written be as $\Delta T \propto e^{\frac{z}{2H}}\chi$, where ΔT is the observed temperature perturbations, z is the altitude and H is the scale height. Trapping may be possible by having three separate regions, with the trapped region in the middle having oscillatory form of temperature perturbations. The other two regions, above and below the region of interest, need to have an exponentially decaying solution. At the equator of Saturn we have observed a nearly-isothermal atmosphere. Above the stellar occultation region, UVS occultations have produced a temperature profile with a positive gradient (H97). Even though observations don't exist both below and above our region of observations, we believe the north polar region which was sensitive to our occultation is a typical "trapped" region. The observed temperature perturbations are oscillatory, and produces the oscillatory behavior in the observed lapse rates. Given the strong evidence on the existence of aerosols in the stratosphere of Saturn at these latitudes, the trapping mechanism is the most likely candidate for the temperature variations observed. Proving that trapping is indeed the reason requires knowledge of the atmosphere both immediately above and below this region, which has not been covered by any of the spacecraft studies.

3.6 Finite Size of the Stellar Sources

Based on the anisotropic refractive scintillation theory as presented by Narayan and Hubbard (1988) we have calculated the projected dimensions of the occulted star. The theory includes three parameters-the projected dimension of the star, a normalization constant for the strength of phase fluctuations in an atmosphere, and an anisotropy parameter. These parameters were determined using the known spike widths of the data and the flux levels they occurred.

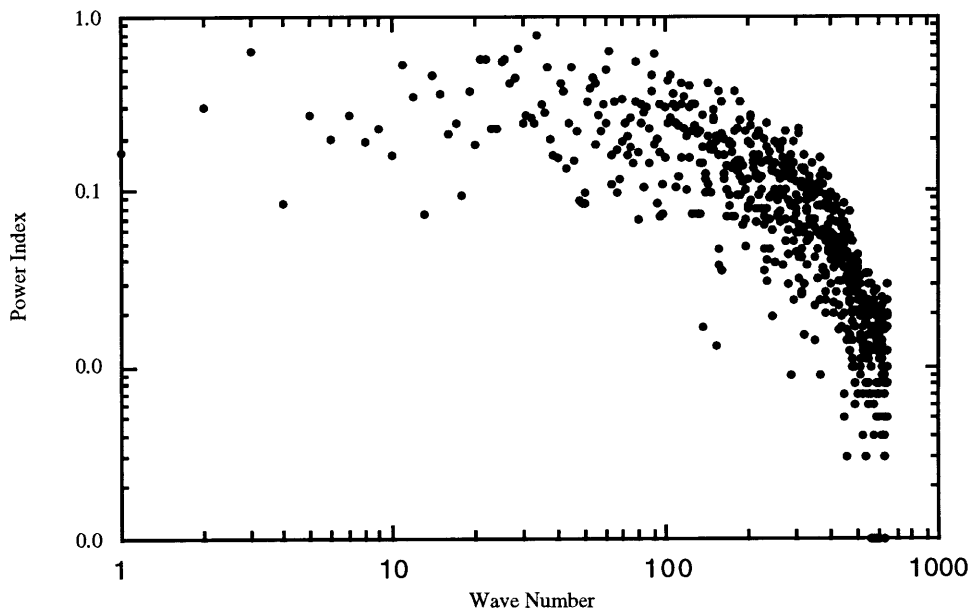
Figure 3.13 Computed power spectrum of light curve residuals for the GSC5249-01240 occultation. We find a power law index, β, of 2.82. Kolmogorov type turbulence in a compressible medium produces fluctuations of index with β=3.66.

The observed power spectrum takes the form

$$Q(q) = Q_0 q^{-\beta} \tag{3.26}$$

where q is the wavenumber of observed fluctuations in the radial direction, and β is the power-law index. For Kolmogorov type turbulences, studied by both Narayan and Hubbard (1988) and French and Lovelace (1983) the observed residuals follow a power law of form $\beta = 11/3$. Figure 3.16 shows the observed power spectrum of 1995 residuals with a best suggested power-law of 2.82. The approximate value of Q_0 for the 1995 data is ~ 1.

Another important parameter in residual studies is the Fresnel scale given by:

$$R_F = \sqrt{2\pi\lambda D}, \tag{3.27}$$

where λ is the wavelength of observations and D is the distance to Saturn. The characteristics of the fluctuations is strongly influenced by phase variations on the scale R_F. A measure of this power can be found through a parameter A given by Goodman and Narayan (1985):

$$A = 2^{2-\beta} g(\beta) Q_0 R_F{}^{\beta-2}, \tag{3.28}$$

where

$$g(\beta) = \frac{\Gamma[(6-\beta)/2]}{\pi(4-\beta)(\beta-2)\Gamma(\beta/2)}. \tag{3.29}$$

For the 1995 data $A \sim 1$ and strong scintillation theory is essential in explaining the observations. Weak scintillation theory is only valid when $A \ll 1$ and is discussed in French and Lovelace (1983). Strong scintillation theory was considered by Narayan and Hubbard (1988) to explain the scintillations observed during the Neptune occultations. Based on the theory presented, the scale of flux in the observer direction, R_r, is given by

$$R_r = \sqrt{2}\left[\sigma_{s0}^2 + \sigma_0^2(\phi^{-2} - 1)^{\frac{12}{5}}\right]^{\frac{1}{2}}$$
(3.34)

where σ_{s0} is the projected size of the stellar source, σ_0 is the normalization constant for the phase fluctuations, and ϕ is the mean flux during immersion. Near the edge of the occultation, the expected width size is constant at a value of $\sqrt{2}\sigma_{s0}$ and increases as a function of the mean flux by $\phi^{-\frac{6}{5}}$. Figure 3.14 plots the observed widths from the 1995 occultation as a function of the mean flux. The best fit line corresponds to the following parameters:

$$\sigma_{s0} = 3.02 \pm 0.22, \quad \sigma_0 = 0.013 \pm 0.019.$$
(3.35)

The parameter σ_{s0} is the projected diameter (FWHM) of the stellar source, based on a Gaussian model for the intensity profile of the star. To relate this parameter to the true stellar diameter one may equate the second moment of the Gaussian profile, $\dfrac{\sigma_{s0}^2}{2}$, to that of a limb-darkened profile (Narayan and Hubbard, 1988). Another approach is to consider an effective one-dimensional intensity profile for the stellar object based on a limb-darkening law of the form, $I(\theta) = (1-b) + b\cos\theta$ (Elliot et al. 1976). Narayan and Hubbard (1986) have calculated the second moment of such a profile for b ranging from 0 to 1 and found that σ_{s0} should be multiplied by a factor between 2.8 and 3.2 to obtain the stellar diameter. This suggests a stellar diameter of 9 km (FWHM) or 0.6 arcsecs.

The parameter σ_0 is related to the strength of the phase fluctuations. This parameter can be used to estimate the relative density fluctuations in Saturn's atmosphere. This value also implies the transition from weak to strong in the 1995 occultation occurred at a mean flux value of 0.01. At this point, the rms. amplitude of phase fluctuations on the Fresnel scale is equal to 1 rad (Narayan and Hubbard, 1988). In comparison the total phase shift, Φ, due to the mean atmosphere is given by

$$\Phi = \frac{H^2}{R_F^2}(\phi^{-2} - 1)$$
(3.36)

66

where H is the scale height and R_F is the Fresnel scale of observations.
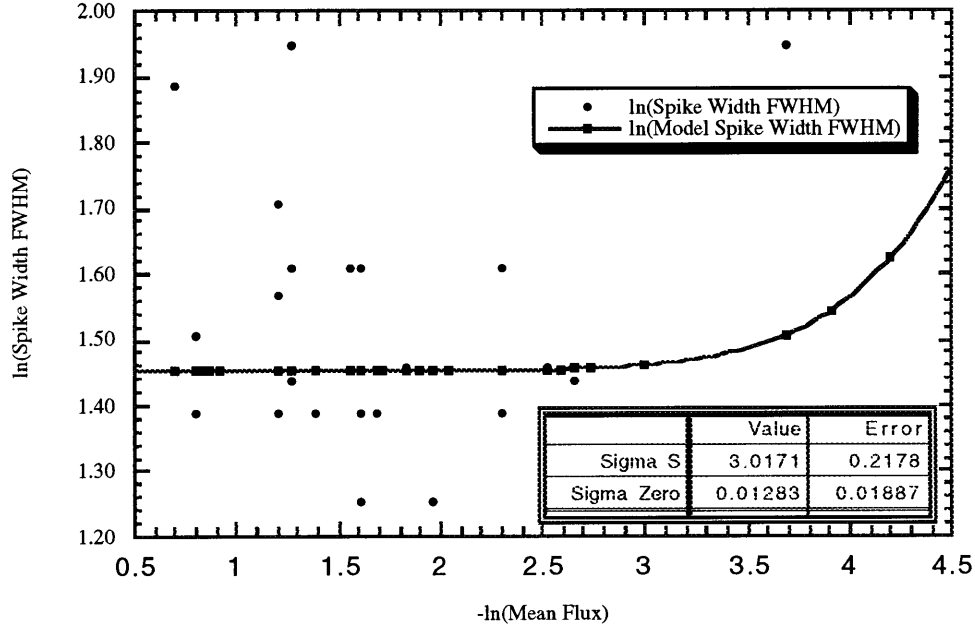

Figure 3.14 Intensity fluctuations as a function of the mean flux during immersion in the 1995 Saturn occultation. The displayed values of R_r are FWHM of the spikes. Solid line corresponds to the modeled widths based on the equation.

Based on the Fresnel scale value, 4.438 km, and mean scale height based on inversions value, 37.5 km, we find the phase shift to be 7.1×10^5. We thus have $\dfrac{\Delta\Phi(R_F)}{\Phi} \sim 1.4 \times 10^{-6}$. The amplitude of the phase fluctuations varies with length scale, R, as $R^{\frac{5}{6}}$ for the Kolmogorov type turbulence in a compressible medium. Thus the relative fluctuations in the projected density Σ vary as $\dfrac{\Delta\Sigma(R)}{\Sigma} \sim 1 \times 10^{-6} R^{\frac{5}{6}}$, where R is in km. We can relate $\dfrac{\Delta\Sigma}{\Sigma}$ to the true space density fluctuations by estimating the number of independent density variations contributing to a given line of sight. The effective thickness of the atmosphere with a radius, $a=54900$ km is

$2(2aH)^{\frac{1}{2}} \sim 4 \times 10^3$. Assuming variations of scale R, the implied fluctuations in the atmospheric density n are

$$\frac{\Delta n(R)}{n} \sim 4 \times 10^{-3} R^{\frac{1}{3}}, \tag{3.37}$$

If the radius scale varies as scale height, then $\dfrac{\Delta n(H)}{n} \sim 1.4\%$.

3.7 Conclusions

The main result of our occultation observations is that the equivalent isothermal temperature of Saturn at a half-light latitude of 84.4 degrees and pressure of 1.54 ± 0.09 μbar is 137 ± 11 K. The radius of Saturn at this half-light level is 54959 ± 10 km. This half-light radius gives information to constrain the planetary figure and study the effect of high zonal winds on Saturn at the pressure level of microbars. The temperature at this level is comparable to the equivalent isothermal temperature near the equator. The temperature profile based on numerical inversion suggests an increase in temperature of 14 K over a vertical length less than a scale height between 6 and 10 μbars, which requires a heating mechanism. We have considered the possibility of aerosol heating in the stratosphere, as the source of energy. The observed scintillations in the GSC5249-01240 light curve can be interpreted based on the gravity wave energy dissipation, which are trapped based on the oscillatory perturbations in the temperature structure. The trapping mechanism considered in this region can easily maintain the aerosols, whose existence has been well observed with HST. Trapped standing waves can also resolve the problem of aerosol transfer and may suggest why the higher latitudinal aerosols have different physical properties with respect to the equatorial aerosols.

We have detected the horizontal temperature structure at the north polar region, where Saturn's polar hexagon has become an interesting topic over the last few years for both observational and theoretical studies. As past occultations probed nearly vertical atmospheric profiles and we now have a nearly horizontal probe, new methods need to be investigated for separating the vertical component from the horizontal component. Future work will address the possibility of separating the horizontal variations from the observed temperature profile. As discussed, due to memory limitations in the instrument

we have lost a significant amount of data from the light curve. We hope that future instruments at major observatories will have better capabilities for recording long, uninterrupted time series for occultation observations.

Appendix A

A1. Gravity

For an object corotating with the atmospheric gas, one must include the effects of both the external gravity field and the centrifugal force when computing the acceleration of gravity. The resulting acceleration (**g**) may be expressed in terms of its radial (g_r) and latitudinal (g_ϕ) components

$$\mathbf{g} = g_r \hat{r} + g_\phi \hat{\phi},$$
(A1)

where $\hat{r}$ and $\hat{\phi}$ are the unit vectors in the radial; and latitudinal directions, respectively. These vector components can be written as

$$g_r(r,\phi) = -\frac{GM}{r^2} + \frac{GM}{r^2}\sum_{i=1}^{\infty}(2i+1)J_{2i}\left(\frac{R}{r}\right)^{2i}P_{2i}(\sin\phi) + \frac{2}{3}\omega^2 r\left[1 - P_2(\sin\phi)\right],$$
(A2)

$$g_\phi(r,\phi) = -\frac{GM}{r^2}\sum_{i=1}^{\infty}J_{2i}\left(\frac{R}{r}\right)^{2i}\frac{dP_{2i}(\sin\phi)}{d\phi} - \frac{1}{3}\omega^2 r\frac{dP_2(\sin\phi)}{d\phi},$$
(A3)

where J_{2i} is the 2ith zonal harmonic constant, R is the radius to which these harmonics are normalized, P_{2i} is the Legendre polynomial of degree 2i, and ω is the angular velocity. The variables r and ϕ denote the distance to the center of mass and the planetocentric latitude respectively. We used the zonal gravity harmonics published by Nicholson and Porco (1988) which were normalized to a radius of 60,300 km (=R). We included the six terms published by them, including the first three that was derived and the rest assumed in their derivation.

At the 1 bar level where there are data on wind velocities for ω we have

$$\omega = \omega_{III} + \frac{V_W}{r\cos\phi}$$
(A4)

70

where V_W is the eastward zonal-wind velocity and ω_{III} is the angular velocity corresponding to the system III rotation period. This period was determined through magnetic field observations of the Saturn by Voyager I and Voyager II and corresponds to 10 hr 39m 22.4s.

Published zonal-wind profiles are available in Smith *et al.* (1982) and Ingersoll and Pollard (1982) where they give V_W as a function of the planetographic latitude, which simply equal to $(\phi + \psi)$ where

$$\psi = \arctan\left(\frac{g_\phi}{g_r}\right). \tag{A5}$$

Assuming a uniformly rotating fluid, the gravity potential ($U(r,\phi)$) may be defined in terms of the gravity by

$$\mathbf{g} = -\nabla U. \tag{A6}$$

The total potential U can be considered in two parts, one due to the gravity (V) and one due to the rotation, which may be either uniform or non-uniform (Ω).

To obtained the simplest solution to derive U following assumptions are made. One by one we will reduce these assumptions to obtain a acceptable gravity field for Saturn.

1. Saturn rotates about a fixed axis with some yet unspecified angular velocity.
2. The system is stationary when viewed an inertial frame of references, and the density of each mass element remains a constant as we follow its motion.
3. No atmospheric drag effects (such as friction).
4. No effect due to the magnetic field of Saturn.

The potential may be obtained by integrating **g** from point of interest (r,ϕ) to a point of infinity on the spin axis:

$$U(r,\phi) - U\left(\infty, \frac{\pi}{2}\right) = \int\limits_{(r,\phi)}^{\left(\infty, \frac{\pi}{2}\right)} g\, ds \tag{A7}$$

71

where *ds* represents an elemental displacement along the path of integration. For a fluid with a uniform angular velocity (corresponding to the system III) rotation, we can write

$$U(r,\phi) = -\frac{GM}{r} + \frac{GM}{r}\sum_{i=1}^{\infty} J_{2i}\left(\frac{R}{r}\right)^{2i} P_{2i}(\sin\phi) - \frac{1}{2}\omega_{III}^2 r^2 \cos^2\phi \qquad (A8)$$

where we have assumed that at infinity potential is equal to zero.

In an iterative manner we can used to above equation to calculate the shape of a reference geoid with polar radius r_p. To do, we will first determine the gravity potential of the reference geoid from above potential equation:

$$U_{ref} = U\left(r_p, \frac{\pi}{2}\right) \qquad (A9)$$

where at the 1 bar level r_p was set equal to 54364 based on the radio occultation observations (Lindal *et al.* 1985). Next we assigned an initial value to $r_{ref}(\phi)$ and the corresponding potential was determined. The error in this potential was then calculated:

$$\Delta U = U(r_{ref},\phi) - U_{ref}. \qquad (A10)$$

This was utilized to compute the correction required in the radius (Δr) at the latitude ϕ:

$$\Delta r = \frac{\Delta U}{g_r}. \qquad (A11)$$

The procedure was then repeated for repeated latitude angles. A zonal wind perturbs the acceleration of gravity at a point (r,ϕ) by an amount $g - g_{ref}$ where g_{ref} is the gravity value with no consideration of zonal winds. That is ignoring the V_w part in the rotational term. V_w may change with altitude, but this derivation assumes that there is no such change. The only reason why this can be justified is by the occultation results such as 28 Sgr where isobaric surfaces appear about equally well at all observed pressure levels. We will come back later on this issue of possibility of winds changing with altitude.

Based on the wind velocities, the perturbed gravity amount can be written as

$$\Delta g_w = V_w \left(2\omega_{III} + \frac{V_w}{r\cos\phi} \right),$$

(A12)

where Δg_w may be thought of as a vector in the meridian plane parallel to the equatorial plane. One may then solve for the altitude of the geoid from the reference geoid through

$$h(\phi) = \frac{1}{g} \int_\phi^{\frac{\pi}{2}} V_w \left[2\omega_{III} + \frac{V_w}{r_{ref}(\phi)\cos\phi} \right] \frac{\sin(\phi + \psi_{ref})}{\cos\psi_{ref}} r_{ref}(\phi)d\phi$$

(A13)

which for small perturbations of the first order can be written as

$$h(\phi) \approx \frac{2\omega_{III}r_p}{g} \int_\phi^{\frac{\pi}{2}} V_w \sin\phi d\phi.$$

(A14)

Which is the same perturbation that is derived similarly through the cylindrical assumption.

73

References

Baron, R. L., R. G. French, and J. L. Elliot 1989. The oblateness of Uranus at the 1 mubar level. *Icarus* 78, 119-130.

Bezard, B., D. Gautier, and B. Conrath 1984. A seasonal model of the Saturnian upper troposphere: Comparison with Voyager infrared measurements. *Icarus* **60**, 274-288.

Bezard, B., and D. Gautier 1985. A seasonal climate model of the atmospheres of the giant planets at the Voyager encounter time. *Icarus* **61**, 296-310.

Bosh, A. S., and S. W. McDonald 1992. Stellar occultation candidates from the Guide Star Catalog. I. Saturn, 1991-1999. *Astron. J.* 103, 983-990.

Bosh, A. S., and C. B. Olkin 1996. Low optical depth features in Saturn's rings: The occultation of GSC5249-01240 by Saturn and its rings. *Bull. Amer. Astron. Soc.* 28, 1124.

Connerney, J. E. P. 1986. Magnetic connection for Saturn's rings and atmosphere. *Geophys. Res. Lett.* 13, 773-776.

Conrath, B. J., D. Gautier, R. A. Hanel, and J. S. Hornstein 1984. The helium abundance of Saturn from Voyager measurements. *Astrophys. J.* 282, 807-815.

Conrath, B. J., and J. A. Pirraglia 1983. Thermal structure of Saturn from Voyager infrared measurements: Implications for atmospheric dynamics. *Icarus* 53, 286-292.

Cooray, A. R., J. L. Elliot, A. S. Bosh, L. A. Young, M. A. Shure 1997. Stellar occultation observations of Saturn's north polar temperature structure. *Icarus,* submitted.

Desch, M. D., and M. L. Kaiser 1981. Voyager measurement of the rotation period of Saturn's magnetic field. *Geophysics Research Letters* 8, 253-256.

Dunham, E., J. L. Elliot, and P. J. Gierasch 1980. The upper atmosphere of Uranus: Mean temperature and temperature variations. *Astrophys. J.* **235**, 274-284.

Elliot, J. L., A. S. Bosh, M. L. Cooke, R. C. Bless, M. J. Nelson, J. W. Percival, M. J. Taylor, J. F. Dolan, E. L. Robinson, and G. W. van Citters 1993. An occultation by Saturn's rings on 1991 October 2-3 observed with the Hubble Space Telescope. *Astron. J.* 106, 2544-2572.

Elliot, J. L., and C. B. Olkin 1996. Probing Planetary Atmospheres with Stellar Occultations. In *Annual Review of Earth and Planetary Sciences* (G. W. Wetherill, Ed.), pp. 89-123. Annual Reviews Inc., Palo Alto.

Elliot, J. L., K. Rages, and J. Veverka 1976. The occultation of b Scorpii by Jupiter. VII. The angular diameters of b Scorpii A_1 and A_2. *Astrophys. J.* 207, 994-1001.

Elliot, J. L., and J. Veverka 1976. Stellar occultation spikes as probes of atmospheric structure and composition. *Icarus* 27, 359-386.

Elliot, J. L., L. H. Wasserman, J. Veverka, C. Sagan, and W. Liller 1974. The occultation of Beta Scorpii by Jupiter. II. The hydrogen-helium abundance in the Jovian atmosphere. *Astrophys. J.* 190, 719-729.

Elliot, J. L., 1989. Does Pluto has a haze layer? in preparation.

Elliot, J. L., and L. A. Young 1992. Analysis of stellar occultation data for planetary atmospheres. I. Model fitting, with application to Pluto. *Astron. J.* 103, 991-1015.

Forrest, W. J., J. L. Pipher, Z. Ninkov, and J. D. Garnett 1990. *InSb DRO Array Characteristics*, Preprint. University of Rochester.

French, R. G., J. L. Elliot, and P. J. Gierasch 1978. Analysis of stellar occultation data. Effects of photon noise and initial conditions. *Icarus* 33, 186-202.

French, R. G., and P. J. Gierasch 1974. Waves in the Jovian upper atmosphere. *J. Atmos. Sci.* 31, 1707-1712.

French, R. G., and R. V. E. Lovelace 1983. Strong turbulence and atmospheric waves in stellar occultations. *Icarus* 56, 122-146.

French, R. G., P. D. Nicholson, M. L. Cooke, J. L. Elliot, K. Matthews, O. Perkovic, E. Tollestrup, P. Harvey, N. J. Chanover, M. A. Clark, E. W. Dunham, W. Forrest, J. Harrington, J. Pipher, A. Barucci, A. Brahic, C. Ferrari, I. Grenier, F. Roques, B. Sicardy, and M. Arndt 1993. Geometry of the Saturn system from the 3 July 1989 occultation of 28 Sgr and Voyager observations. *Icarus* 103, 163-214.

Friedson, A. J. 1994. Gravity waves in Titan's atmosphere. *Icarus* 109, 40-57.

Goodman, J., and R. Narayan 1985. Slow pulsar scintillation and the spectrum of the interstellar electron density fluctuations. *Mon. Not. Roy. Astron. Soc.* 214, 519-537.

Hanel, R., B. Conrath, F. M. Flasar, V. Kunde, W. Maguire, J. Pearl, J. Pirraglia, R. Samuelson, L. Herath, M. Allison, D. Cruikshank, D. Gautier, P. Gierasch, L. Horn, R. Koppany, and C. Ponnamperuma 1981. Infrared observations of the Saturnian system from Voyager 1. *Science* 212, 192-200.

Hanel, R., B. Conrath, F. M. Flasar, V. Kunde, W. Maguire, J. Pearl, J. Pirraglia, R. Samuelson, L. Herath, M. Allison, D. Cruikshank, D. Gautier, P. Gierasch, L. Horn, R. Koppany, and C. Ponnamperuma 1982. Infrared observations of the Saturnian system from Voyager 2. *Science* **215**, 544-548.

Harrington, J., M. L. Cooke, W. J. Forrest, J. L. Pipher, E. W. Dunham, and J. L. Elliot 1993. IRTF observations of the occultation of 28 Sgr by Saturn. *Icarus* 103, 235-252.

Harrington, J., E. W. Dunham, W. J. Forrest, and J. L. Pipher 1989. IRTF infrared imaging observation of the occultation of 28 Sgr by Saturn. *Bull. Amer. Astron. Soc.* 21, 954.

Hubbard, W. B., V. Haemmerle, C. C. Porco, G. H. Rieke, and M. J. Rieke 1995. The occultation of SAO 78505 by Jupiter. *Icarus* 113, 103-109.

Hubbard, W. B., D. M. Hunten, H. J. Reitsema, N. Brosch, Y. Nevo, E. Carreira, F. Rossi, and L. H. Wasserman 1990. Results for Titan's atmosphere from its occultation of 28 Sagittarii. *Nature* 343, 353-355.

Hubbard, W. B., C. C. Porco, D. M. Hunten, G. H. Rieke, M. J. Rieke, D. W. McCarthy, V. Haemmerle, R. Clark, E. P. Turtle, J. Haller, B. McLeod, L. A. Lebofsky, R. Marcialis, J. B. Holberg, R. Landau, L. Carrasco, J. Elias, M. W. Buie, S. E. Persson, T. Boroson, S. West, and D. J. Mink 1993. The occultation of 28 Sgr by Saturn: Saturn pole position and astrometry. *Icarus* 103, 215-234.

Hubbard, W. B., C. C. Porco, D. M. Hunten, G. H. Rieke, M. J. Rieke, D. W. McCarthy, V. Hammerle, J. Haller, B. McLeod, L. A. Lebofsky, R. Marcialis, J. B. Holberg, R. Landau, L. Carrasco, J. Elias, M. W. Buie, E. W. Dunham, S. E. Persson, T. Botoson, S. West, R. G. French, J. Harrington, J. L. Elliot, W. J. Forrest, J. L. Pipher, R. J. Stover, B. Sicardy, and A. Brahic 1997. Structure of Saturn's mesosphere from the 28 Sgr occultations. submitted.

Hubbard, W. B., and D. J. Stevenson 1984. Interior structure of Saturn. In *Saturn* (T. Gehrels and M. S. Matthews, Ed.), pp. 47-87. University of Arizona Press, Tucson.

Hunten, D. M., and J. Veverka 1976. Stellar and spacecraft occultations by Jupiter: A critical review of derived temperature profiles. In *Jupiter* (T. Gehrels, Ed.), pp. 247-283. University of Arizona Press, Tucson.

Ingersoll, A. P., R. F. Beebe, B. J. Conrath, and G. E. Hunt 1984. Structure and dynamics of Saturn's atmosphere. In *Saturn* (T. Gehrels and M. Matthews, Ed.), pp. 195-238. University of Arizona Press, Tucson.

Jenkner, H., B. M. Lasker, C. R. Sturch, B. J. McLean, M. M. Shara, and J. L. Russell 1990. The Guide Star Catalog. III. Production, database organization, and population statistics. *Astron. J.* 99, 2082 - 2154.

Kaiser, M. L., M. D. Desch, W. S. Kurth, A. Lecacheux, F. Genova, B. M. Pedersen, and D. R. Evans 1984. Saturn as a radio source. In *Saturn* (T. Gehrels and M. S. Matthews, Ed.), pp. 378-415. University of Arizona Press, Tucson.

Karkoschka, E., and M. G. Tomasko 1993. Saturn's upper atmospheric hazes observed by the Hubble Space Telescope. *Icarus* 106, 428-441.

Lasker, B. M., C. R. Sturch, B. J. McLean, J. L. Russell, H. Jenkner, and M. M. Shara 1990. The Guide Star Catalog. I. Astronomical foundations and image processing. *Astron. J.* 99, 2019 - 2058.

Lindal, G. F., D. N. Sweetnam, V. R. Eshlemaa 1985. The atmosphere of Saturn: an analysis of the Voyager radio occultation measurements. *Astron. J.* 90, 1136-1146.

Lindzen, R. S., and D. Blake 1971. Internal gravity wars in atmospheres with realistic dissipation and temperature Part II. Thermal tides excited below the mesopause. *Geophys. Fluid Dynamics* 2, 31-61.

Narayan, R., and W. B. Hubbard 1988. Theory of anisotropic refractive scintillation: Application to stellar occultations by Neptune. *Astrophys. J.* 325, 503-518.

Nicholson, P. D., C. McGhee, and R. G. French 1995. Saturn's central flash from the 3 July 1989 occultation of 28 Sgr. *Icarus* 113, 57-83.

Nicholson, P. D., and C. Porco 1988. A new constraint on Saturn's zonal gravity harmonics from Voyager observations of an eccentric ringlet. *J. Geophys. Res.* 93, 10209-10224.

Olkin, C. B. 1996. *Stellar occultation studies of Triton's atmosphere.* Ph. D. Thesis, Department of Earth, Atmospheric, and Planetary Sciences, Massachusetts Institute of Technology, Cambridge.

Orton, G. S., A. P. Ingersoll, 1980. Saturn's atmospheric temperature structure and heat budget. *J. Geophys. Res.* **85,** 5871-5881.

Rizk, B., and D. M. Hunten 1990. Solar heating of the Uranian mesopause by dust of ring origin. *Icarus* **88**, 429-447.

Roberge, A. 1996. *Investigation of the Orbits of the Saturnian Satellites during a Ring-Plane Crossing.* S. B. Thesis, Department of Physics, Massachusetts Institute of Technology, Cambridge.

Roques, F., B. Sicardy, R. G. French, W. B. Hubbard, A. Barucci, P. Bouchet, A. Brahic, J.-A. Gehrels, T. Gehrels, I. Grenier, T. Lebertre, J. Lecacheux, J. P. Maillard, R. A. McLaren, C. Perrier, F. Vilas, and M. D. Waterworth 1994. Neptune's upper stratosphere, 1983-

1990: Ground-based stellar occultation observations. *Astron. & Astrophys.* 288, 985-1011.

Russell, J. L., B. M. Lasker, B. J. McLean, C. R. Sturch, and H. Jenkner 1990. The Guide Star Catalog. II. Photometric and astrometric models and solutions. *Astron. J.* 99, 2059 - 2081.

Sanchez-Lavega, A., J. Lecacheux, F. Colas, P. Laques 1993. Ground-based observations of Saturn's north polar spot and hexagon. *Science* **260**, 329-332.

Sanchez-Lavega, A., J. Lecacheux, F. Colas, J. F. Rojas, J. R. Acarreta 1996. New observations of the long-lived Saturn's north polar spot: 1992-1995. *Bull. Amer. Astron. Soc.* **28**, 1128.

Shure, M., D. W. Toomey, J. T. Rayner, P. M. Onaka, and A. T. Denault 1994. *NSFCAM: A new infrared array camera for the NASA Infrared Telescope Facility.* Instrumentation in Astronomy VIII, Kona, HI, pp 25-33.

Sicardy, B., A. Brahic, C. Ferrari, D. Gautier, J. Lecacheux, E. Lellouch, F. Roques, J. E. Arlot, F. Colas, W. Thuillot, F. Sevre, J. L. Vidal, C. Blanco, S. Cristaldi, C. Buil, A. Klotz, and E. Thouvenot 1990. Probing Titan's atmosphere by stellar occultation. *Nature* 343, 350-353.

Sicardy, B., M. Combes, J. Lecacheux, P. Bouchet, A. Brahic, P. Laques, C. Perrier, L. Vapillon, and Y. Zeau 1985. Variations of the stratospheric temperature alont the limb of Uranus: Results of the 22 April 1982 stellar occultation. *Icarus* 64, 88-106.

Smith, B. A., L. Soderblom, R. Batson, P. Bridges, J. Inge, H. Masursky, E. Shoemaker, R. Beebe, J. Boyce, G. Briggs, A. Bunker, S. A. Collins, C. J. Hansen, T. V. Johnson, J. L. Mitchell, R. J. Terrile, A. F. I. Cook, J. Cuzzi, J. B. Pollack, J. B. Danielson, A. P. Ingersoll, M. E. Davies, G. E. Hunt, D. Morrison, T. Owen, C. Sagan, J. Veverka, R. Strom, and V. E. Suomi 1982. A new look at the Saturn system: The Voyager 2 images. *Science* 215, 504-537.

Smith, G. R., D. E. Shemansky, J. B. Holberg, A. L. Broadfoot, B. R. Sandel, and J. C. McConnell 1983. Saturn's upper atmosphere from the Voyager 2 EUV solar and stellar occultations. *J. Geophys. Res.* 88, 8667-8678.

Smith, J. D. 1995. *Lunar occultation timing in a two-telescope observation of Saturn.* B. S. Thesis, Department of Physics, Massachusetts Institute of Technology, Cambridge.

STScI 1989. The Guide Star Catalog.

Taylor, G. E. 1983. I.A.U. commission 20 working group on the prediction of occultations. *Satellites and Minor Planets Bulletin* 30,

Tyler, G. L., D. N. Sweetnam, J. D. Anderson, J. K. Campbell, V. R. Eshleman, D. P. Hinson, G. S. Levy, G. F. Lindal, E. A. Marouf, and D. P. Hinson 1986. Voyager 2 radio science observations of the Uranian system: Atmosphere, rings, and satellites. *Science* 233, 79-84.

Walterschied, R. L., and G. Shubert 1990. Nonlinear evolution of an upward propagating gravity wave: Overturning, convection, transience, and turbulence. *J. Atmos. Sci.* **47**, 101-125.

Wasserman, L. H., and J. Veverka 1973. Analysis of spikes in occultation curves: A critique of Brinkmann's method. *Icarus* 18, 599-604.

Yelle, R. V., L. A. Young, R. J. Vervack, R. Young, L. Pfister, and B. R. Sandel 1996. The structure of Jupiter's upper atmosphere: Predictions for Galileo. *J. Geophys. Res.* **101**, 2149-2161.

Young, A. T. 1976. Scintillations during occultations by planets. I. An approximate theory. *Icarus* **27**, 335-357.

Young, L. A., R. V. Yelle, R. E. Young, A. Seiff, and D. B. Kirk 1996. Gravity waves in Jupiter's upper atmosphere. *Bull. Amer. Astron. Soc.* **28**,